Editors' Suggestion

Hessian characterization of the pinning landscape in a type-II superconductor

R. Willa[1,2] V. B. Geshkenbein[3] and G. Blatter[3]
[1]*Institute for Theory of Condensed Matter, Karlsruhe Institute of Technology, 76131 Karlsruhe, Germany*
[2]*Heidelberger Akademie der Wissenschaften, 69117 Heidelberg, Germany*
[3]*Institute for Theoretical Physics, ETH Zurich, 8093 Zurich, Switzerland*

(Received 27 July 2021; revised 18 February 2022; accepted 22 February 2022; published 11 April 2022)

Recent advances in vortex imaging allow for tracing the position of individual vortices with high resolution. Pushing an isolated vortex through a superconducting sample with the help of a controlled *dc* transport current and measuring its local *ac* response, the pinning energy landscape could be reconstructed along the vortex trajectory [L. Embon *et al.*, Sci. Rep. **5**, 7598 (2015)], providing unprecedented access to the mesoscopic, i.e., sample dependent, properties of a superconducting device. The controlled motion of objects through such tilted energy landscapes is fundamentally limited to those areas of the landscape developing local minima under appropriate tilt. We introduce the Hessian stability map and the Hessian character of a pinning landscape as quantities that help characterizing a pinning landscape, or short, pinscape. We determine the Hessian character, the area fraction admitting stable vortex positions, for various types of pinning potentials: Assemblies of cut parabolas, Lorentzian- and Gaussian-shaped traps, as well as a Gaussian random disordered energy landscape, with the latter providing a universal result of $(3-\sqrt{3})/6 \approx 21\%$ of stable area. Our Hessian analysis sheds light on various aspects of mesoscopic vortex physics in the single vortex limit and opens interesting avenues in strong pinning theory.

DOI: 10.1103/PhysRevB.105.144504

I. INTRODUCTION

The recent years have seen an astounding progress in the ability to image vortices in superconductors [1–5]. The high accuracy of these local-probe techniques allow to study the shape of individual vortices [5] and even manipulate them, e.g., via magnetic forces [6,7] or local mechanical stress [8]. A new quality in precision-imaging has been achieved using a novel SQUID-on-Tip (SOT) device combined with *ac*/*dc* techniques [9,10]. Changing the current drive in the sample allows to push and trace individual vortices and thereby extract the shape of the energy landscape (pinning landscape or simply pinscape) from measured SOT data. Such information is most welcome in optimizing pinscapes, which in turn is of great technological interest for high-current applications [11,12]. Furthermore, the experiment opens new avenues in mesocopic vortex physics: While the engineering of pinscapes through introduction of antidots [13], magnetic particles [14,15], or changes in sample geometry [16–18] allow for a deliberate manipulation of vortex matter, the SOT imaging in Ref. [9] or the Bitter decoration in Ref. [19] allow to access the pinscape in naturally grown samples. In analogy to the well-known *ball-in-a-maze* dexterity game [20], where a ball is driven through a maze by controlling the tilt of the plane, we refer to the experiment in Ref. [9] as a vortex-in-a-maze.

In the experiment of Ref. [9], a vortex (carrying a quantum $\Phi_0 = hc/2e$ of magnetic flux) is driven across a two-dimensional superconducting strip made from lead (Pb). The variations of the vortex energy across the strip defines the pinning landscape where the vortex can be trapped in local minima, see Fig. 1. These local minima can be manipulated by applying a transport current j along the constriction (the y axis) that tilts the potential landscape in the transverse direction (parallel to the x axis). A small *ac* current imposed on top of the *dc* drive allows for the precise tracking of the vortex position. The reconstruction of vortex tracks in Ref. [9] has brought forward interesting observations in the vortex dynamics that is dominated by the shape of the pinscape: For one, a very large *ac* displacement amplitude in the middle

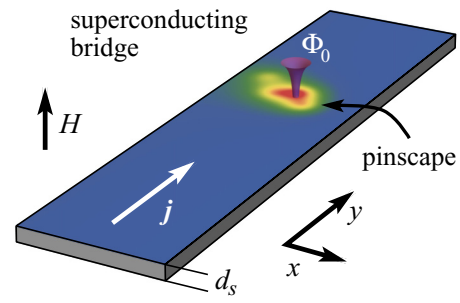

FIG. 1. Setup for carrying out the vortex-in-a-maze experiment in Ref. [9]. A superconducting film of thickness d_s of order of the coherence length (and of the penetration depth) is subject to an external field H producing vortices in the film. The colored area illustrates the depth of the pinning energy potential (with deep regions marked in red) as inferred from the experiment. The current density $\boldsymbol{j} \| \hat{\boldsymbol{y}}$ drives the vortex along the $\hat{\boldsymbol{x}}$ direction. Different entry points along the $\hat{\boldsymbol{y}}$ direction allow to probe other parts of the pinscape

of the trapping well suggests a strong local softening of the confining potential, while the abrupt departure of the vortex from the defect—with no significant softening and absence of a maximum in the pinning force—has inspired the "broken-spring" effect reported in Ref. [9]. These observations find a natural explanation in our Hessian analysis of the pinscape.

The present paper addresses the central question, what regions of the pinscape can be probed at all, i.e., which points in the plane allow for a local minimum in the (tilted) potential landscape—this question will take us to the *Hessian stability map* of the disorder potential, see Fig. 2 below. A quantitative question then arises about the total area fraction of the pinning landscape where a vortex can be stabilized, given the appropriate (linear) force. This question is addressed by the calculation of the *Hessian character*. We determine this quantity for various types of pinning landscapes, a random distribution of cut parabolic wells and of Lorentzian- and Gaussian-shaped pins of given density; such traps are often used in numerical work [21,22] on vortex pinning and dynamics. Furthermore, we study the case of a Gaussian random potential landscape for which we find the universal result $(3-\sqrt{3})/6 \approx 21\%$ of stable area fraction; This type of potential is typically used in the context of analytical work on random manifolds [23] and disorder-induced pinning [24–26]. Beyond quantifying the fitness of a landscape to pin vortices, the Hessian characterization is relevant in the context of strong-pinning theory, thus making it a valuable asset in the field of (mesoscopic) vortex matter physics.

The Hessian matrix of random landscapes has been studied in different contexts, ranging from more abstract discussions of the statistics of critical points (where gradients vanish) of Gaussian fields in high-dimensional spaces [27,28] or topological rules for their arrangement in a random phase field [29], to more specific analyses of the intensity of laser speckle patterns [30] or the complexity of the free energy function in a model glass [31], see Ref. [28] for an extended list of references. Here, we focus on a planar energy landscape where we are interested in its stable area, i.e., the collection of all points that can become minima under appropriate tilt, rather than studying the (spectral) distribution of individual critical points (minima, maxima, and saddles).

Before entering our study of the Hessian map and character, we briefly discuss in Sec. II the pinscape spectroscopy used in the reconstruction of the pinning landscape [9] and discuss the "spring-softening" and "broken-spring" effects in the light of our Hessian pinscape analysis. The definition of the Hessian stability map in Sec. III then follows quite naturally and we discuss its various relations to the pinscape spectroscopy of Ref. [9]. In Sec. IV, we focus on the main topic of this paper, the determination of the Hessian character of various types of pinscapes, i.e., a random distribution of various defect potentials of different shapes as well as the case of a Gaussian random potential landscape. As a side result of our analysis, we show in Appendix D how such a Gaussian random landscape can be obtained as the dense limit of overlapping defects with the correlator given through the convolution of two shifted defect potentials. Section V provides a short summary, including an extension of our Hessian analysis to natural (alpine and plane) landscapes (Switzerland and The Netherlands), where we find that their Hessian coefficients are surprisingly close to those of a Gaussian random landscape.

II. PINSCAPE SPECTROSCOPY

We motivate our study of the Hessian stability map and the Hessian character of a pinscape with a brief reminder of the setup and technique discussed in Ref. [9], see Fig. 1, where the pinning landscape of vortices in a type-II superconducting film has been imaged with the help of a SOT device. In this experiment, an isolated vortex residing in a superconducting film of thickness d_s (comparable to the superconducting coherence length and the London penetration length) is trapped by a spatially varying potential landscape $U(\boldsymbol{r})$, where $\boldsymbol{r} = (x, y)$ is the planar coordinate. Given the weak field strength of 3 Gauss used in the experiment [9], only one (Pearl [32]) vortex is present in the sample, justifying our assumption of the vortex as an isolated object; we will discuss the effect of interactions at moderate fields later below. Applying a current $\boldsymbol{j}$ along the $\hat{\boldsymbol{y}}$ direction of the film, the total force $\boldsymbol{F}$ acting on the vortex involves the two contributions $\boldsymbol{F} = \boldsymbol{F}_{\rm pin} + \boldsymbol{F}_{\rm L}$, where $\boldsymbol{F}_{\rm pin} = -\nabla U(\boldsymbol{r})$ accounts for the potential landscape and $\boldsymbol{F}_{\rm L} = \Phi_0 j d_s \hat{\boldsymbol{x}}/c$ is the current-induced Lorentz force. The Lorentz force effectively tilts the pinscape $U(\boldsymbol{r}) \to U_{\rm tilt}(\boldsymbol{r}, F_{\rm L}) = U(\boldsymbol{r}) - F_{\rm L} x$ in the $\hat{\boldsymbol{x}}$ direction.

Besides the excellent resolution of the SOT device, the precise determination of the vortex position in the vortex-in-a-maze experiment [9] relies on a shaking technique where an additional small oscillatory ac current $j_{ac}\exp(-i\omega t)$ is applied on top of the dc drive. The vortex trajectory $\boldsymbol{u}(t)$ then is governed by the dissipative equation of motion

$$\eta \dot{\boldsymbol{u}} = \boldsymbol{F}(\boldsymbol{u}, t), \tag{1}$$

with η the viscosity and $\boldsymbol{F} = \boldsymbol{F}_{\rm pin} + \boldsymbol{F}_{\rm L} + \boldsymbol{F}_{ac}\exp(-i\omega t)$ the total force acting on the vortex. By applying a sequence of increasing dc tilts $F_{{\rm L}n}$, the vortex will move forward through the pinscape and oscillate around a tilt-dependent minimum $\boldsymbol{r}_n(F_{{\rm L}n})$. Near this position, the associated energy profile can be expanded in the displacement $\boldsymbol{u} = \boldsymbol{r} - \boldsymbol{r}_n$,

$$U_{\rm tilt}(\boldsymbol{r}, F_{{\rm L}n}) = U_{\rm tilt}(\boldsymbol{r}_n, F_{{\rm L}n}) + a_n u_x^2 + b_n u_y^2 + c_n u_x u_y, \tag{2}$$

with higher-order corrections becoming relevant near the edges of the stable regions. The local curvatures $a_n = a(\boldsymbol{r}_n)$, $b_n = b(\boldsymbol{r}_n)$, and $c_n = c(\boldsymbol{r}_n)$ define the Hessian matrix via Eq. (13), see below.

Expressing the vortex displacement through $\boldsymbol{u} = (u_x, u_y)\, e^{-i\omega t}$, the equation of motion (1) takes the form

$$i\eta\omega u_x = 2a u_x + c u_y - F_{ac}, \tag{3}$$

$$i\eta\omega u_y = 2b u_y + c u_x. \tag{4}$$

These equations can be solved and analyzed perturbatively in the small parameter $\eta\omega/U''$ involving the viscous term $\eta\omega$ and the curvatures $U'' \sim a, b, c$; indeed, simple estimates (see Appendix A) show that this ratio is small for the material and setup in Ref. [9]. Solving Eqs. (3) and (4) and expanding the result to lowest (0th) order in $\eta\omega/U''$, we find that

$$u_x = \frac{F_{ac}}{2a(1 - c^2/4ab)} \quad \text{and} \quad u_y = (-c/2b)u_x. \tag{5}$$

The motion is in phase with the external driving force and follows the local potential minimum. Hence, although the *ac* force is applied along $\hat{\boldsymbol{x}}$, the vortex oscillates at a finite angle $\phi = \arctan(u_y/u_x) = -\arctan(c/2b)$ away from the $\hat{\boldsymbol{x}}$ axis in the direction of its trajectory.

Given the displacement amplitudes u_x and u_y, one easily reconstructs the potential along the vortex trajectory. For the specific choice of linear increments $F_{\text{L}n} = nF_{ac}$ [9], the equilibrium position $\boldsymbol{r}_n$ at the drive $F_{\text{L}n}$ relates to the position $\boldsymbol{r}_{n-1}$ via

$$\boldsymbol{r}_n = \boldsymbol{r}_{n-1} + (u_{x,n-1}, u_{y,n-1}), \tag{6}$$

where $u_{x,n}$, $u_{y,n}$ are the *ac* displacement amplitudes (5) measured at the drive $F_{\text{L}n}$. This trivial iterative relation leads to the trajectory $\boldsymbol{r}_n = \sum_{m=0}^{n-1}(u_{x,m}, u_{y,m})$. Combining the definition of the tilted potential U_{tilt} at $F_{\text{L}n} = nF_{ac}$ with the quadratic approximation (2), we obtain

$$\begin{aligned} U^n_{\text{tilt}}(x,y) &= U(x,y) - nF_{ac}x \\ &\approx U^n_{\text{tilt}}(x_n,y_n) + a_n(x-x_n)^2 + b_n(y-y_n)^2 \\ &\quad + c_n(x-x_n)(y-y_n). \end{aligned} \tag{7}$$

Solving for $U(x_{n-1}, y_{n-1})$ and $U(x_n, y_n)$ and combining the results with Eqs. (5) and (6), one finds the change in the pinning potential between neighboring points [we choose the arbitrary offset $U(\boldsymbol{r}_0) = 0$],

$$U(x_n, y_n) \approx U(x_{n-1}, y_{n-1}) + (n - 1/2)\, u_{x,n-1} F_{ac} \tag{8}$$

and its iteration provides us with potential

$$U(\boldsymbol{r}_n) \approx F_{ac} \sum_{m=0}^{n-1} (m + 1/2)\, u_{x,m}. \tag{9}$$

The reconstruction of the pinscape along a trajectory in 2D only involves a 1D integral along $\hat{\boldsymbol{x}}$, a consequence of the unidirectional tilt. Indeed, the implicit stability criterion along $\hat{\boldsymbol{y}}$, $\partial U/\partial y = 0$, reduces the integration in the xy plane to the simple 1D form of Eq. (8).

Given the unidirectional nature of the Lorentz force $\mathbf{F}_{\text{L}} \parallel \hat{\boldsymbol{x}}$, the ensuing one dimensionality of the trajectory is complicating the task of mapping out the two-dimensional potential landscape. One possible way out is to induce a local motion along $\hat{\boldsymbol{y}}$ with the help of a high-frequency *ac* drive and measuring the out-of-phase response signal; this technique allows to expand the probing region in the $\hat{\boldsymbol{y}}$ direction but may be quite demanding, depending on the material and experimental parameters. In fact, the solution and subsequent expansion of Eqs. (3) and (4) to linear order in $\eta\omega/U''$ provides an out-of-phase correction δu_x, $\delta u_y \propto i(\eta\omega/U'')/U''$ that could be measured independently, at least in principle. The four displacements u_x, u_y, δu_x, and δu_y then allow for the determination of all local curvatures

$$a = \frac{F_{ac}}{2u_x}\left[1 + \frac{u_y^2/u^2}{(\delta u_y/u_y)(u_x/\delta u_x) - 1}\right], \tag{10}$$

$$b = \frac{F_{ac}}{2u_x}\frac{u_x^2/u^2}{(\delta u_y/u_y)(u_x/\delta u_x) - 1}, \tag{11}$$

$$c = \frac{F_{ac}}{2u_x}\frac{-2u_xu_y/u^2}{(\delta u_y/u_y)(u_x/\delta u_x) - 1}, \tag{12}$$

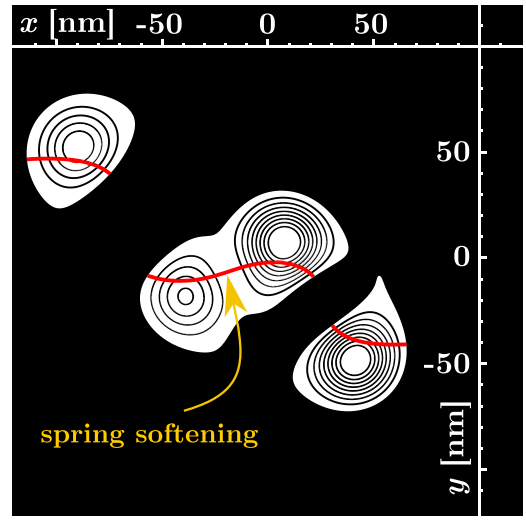

FIG. 2. A view on the pinning landscape through the Hessian stability map. Shown is the example of the pinscape derived from measurements in Ref. [9], see Fig. 5(a) therein. All of the black area is unstable, i.e., the Hessian matrix Eq. (13) has at least one negative eigenvalue; vortices cannot be trapped at any point within this region and the potential landscape cannot be probed. A position within the white area is stable and turns into a local minimum for a specific tilt along $\hat{\boldsymbol{x}}$ and $\hat{\boldsymbol{y}}$. Contour lines show equi-Hessians where $\det H = 0.3k\,(\text{meV/nm}^2)^2$ for integer k. For a unidirectional tilt along $\hat{\boldsymbol{x}}$, only one specific trajectory (red) is accessible within the stable regions. Close to the border of the stable regions, the Hessian becomes small and the *ac* response of the vortex increases. The divergence of the *ac* displacement at the Hessian boundary is preempted by the thermal activation out of the well and subsequent runaway of the vortex across the unstable region. At the center of the double defect (yellow arrow) the vortex goes though a flat region with a small Hessian, implying a large *ac* response ("spring softening") as observed in Fig. 2(e) of Ref. [9].

where $u = (u_x^2 + u_y^2)^{1/2}$ is the total displacement amplitude. This provides access to the local reconstruction of the potential $U(x, y)$ within a strip around the trajectory; more details of this extension of pinscape spectroscopy are presented in Appendix B.

III. HESSIAN STABILITY MAP

Given the possibility to map out the pinning potential of a film through pinscape spectroscopy, the question poses itself which part of the plane can actually be analyzed in this manner and what happens at the boundaries of these areas; the answer to these questions is given by the Hessian stability map.

In the absence of an *ac* current, the vortex resides in a minimum of the tilted potential $U_{\text{tilt}}(\boldsymbol{r}, F_{\text{L}})$. Such a *stable point* is characterized by a vanishing first derivative along both $\hat{\boldsymbol{x}}$ and $\hat{\boldsymbol{y}}$ (no net force) and a positive curvature. The second condition is satisfied, if the Hessian matrix

$$H(x,y) = \begin{pmatrix} \frac{\partial^2 U}{\partial x^2} & \frac{\partial^2 U}{\partial x \partial y} \\ \frac{\partial^2 U}{\partial y \partial x} & \frac{\partial^2 U}{\partial y^2} \end{pmatrix} = \begin{pmatrix} 2a(x,y) & c(x,y) \\ c(x,y) & 2b(x,y) \end{pmatrix} \tag{13}$$

is positive definite, i.e., it has a positive determinant

$$\det H(x,y) = 4a(x,y)b(x,y) - c^2(x,y) > 0 \qquad (14)$$

and a positive trace

$$\mathrm{tr}H(x,y) = 2[a(x,y) + b(x,y)] > 0. \qquad (15)$$

Here, the coefficients $a(\boldsymbol{r})$, $b(\boldsymbol{r})$, and $c(\boldsymbol{r})$ coincide with the local expansion coefficients in Eq. (2). While Eq. (14) excludes indefinite matrices (saddle-point solutions), the positive trace (15) additionally discards negative-definite Hessian matrices (potential maxima). Note that the Hessian does not depend on the (linear) drive, hence it characterizes the pinscape $U(x,y)$ itself, rather than the forced pinscape U_{tilt}. As such, the Hessian matrix with its determinant and trace provides information on the potential's capability of stabilizing a vortex at a specific point $\boldsymbol{r}$ of the plane upon application of the appropriate tilt.

The traditional way of studying the potential landscape is via equipotential (or elevation) maps. They depend on the current-induced tilt and their minima tell about possible (meta)stable positions for the vortex. Adopting a global view, the Hessian matrix helps separating stable points from unstable points. This way, the two-dimensional pinning landscape can now be divided into stable areas characterized by the set of conditions $\det H(x,y) > 0$ and $\mathrm{tr}H(x,y) > 0$, and unstable ones where at least one condition is violated. We thus introduce the *Hessian stability map*, i.e., the graphical representation of the pinscape regions associated with stable points, as a tool to characterize a potential landscape, with a "good" pinscape described by a large percentage of stable area. In Fig. 2, we show, for illustration, the stability region, together with equi-Hessian contour lines, for the potential landscape mapped out in Ref. [9] [see Fig. 5(a) therein] and also shown in the setup in Fig. 1. Within the black regions, at least one eigenvalue is negative, implying that this position cannot be made a stable vortex position for any tilt (in either $\hat{\boldsymbol{x}}$ or $\hat{\boldsymbol{y}}$ direction). In the following, we briefly discuss the role played by the Hessian map in the context of pinscape spectroscopy via *ac* and *dc* forces. In Sec. IV, we assume an extended view on the problem and determine the Hessian character, i.e., the area fraction of stable regions, for different potential landscapes often used in numerical or analytical studies of vortex pinning and dynamics. These are a finite density of cut parabolas, of Gaussian- and Lorentzian-shaped potentials, as well as a Gaussian random potential.

Let us first interpret the Hessian stability map and extract some physical insights into the pinscape. Focusing on the boundaries in the stability map, we note that the vortex displacement $\boldsymbol{u} \propto (1 - c^2/4ab)^{-1}$ diverges, as $c^2 \to 4ab$ when the minimum in $\boldsymbol{r}_n$ approaches the boundary, see Eq. (5). Upon approaching the singular point $c^2 = 4ab$, the expression for the trajectory's angle ϕ simplifies to $\phi = \arctan[(a/b)^{1/2}]$ and thus provides access to the ratio of the potential curvatures along the directions $\hat{\boldsymbol{x}}$ and $\hat{\boldsymbol{y}}$. Interesting features show up when multiple defects combine into a more complex pinning landscape [9]. For example the vortex can approach the depinning point of one defect and transit to another without entering the unstable region of the pinscape. The pinscape then develops a flat region with a small Hessian determinant in the middle of the well. As a result, the *ac* displacement amplitude rises steeply as observed in Ref. [9], what corresponds to a *spring softening* as highlighted in Fig. 2, arrow. Analyzing the vortex trajectory in the central defect more carefully, one notes that the vortex traverses (from left to right) a region going from $\det H \sim 1$ $(\mathrm{meV/nm^2})^2$ near the first minimum, to a small value below 0.3 $(\mathrm{meV/nm^2})^2$ near the "saddle", to a large value $\sim$2 $(\mathrm{meV/nm^2})^2$ in the second minimum. One thus expects an enhancement of the *ac* amplitude by a factor of 3–4 starting at the left of the spring softening and a factor 7–8 relative to the value at the right side, in qualitative agreement with the experiment.

Another aspect of interest is the escape of the vortex from the stable regime. The proper understanding of this phenomenon requires to include higher-order terms in the local expansion of the potential $U(x,y)$ and involves thermal escape over barriers and possibly anharmonic effects, see Appendix C for details. Our semiquantitative analysis of the setup in Ref. [9] confirms that thermal fluctuations are strong and trigger the escape of the vortex from the stable region at a quite large distance away from the stability boundary, in agreement with the discussion of the "broken-spring" effect in the experiment. Specifically, thermal fluctuations and vortex escape do cut off the expected divergence in the displacement $\boldsymbol{u} \propto (1 - c^2/4ab)^{-1}$ and the reconstructed pinning force does not go through a maximum at the point of escape.

So far, we have motivated the origin and practical usefulness of our Hessian analysis in the single vortex limit and with emphasis on the mesoscopic aspect of vortex physics. Going beyond this single vortex limit, one may include the effect of other vortices in the sample with the help of the so-called cage potential $U_{\mathrm{cage}}(r) \approx \pi\varepsilon_0(r/a_0)^2$ that is generated by the neighboring vortices in the lattice [33,34]; here, $\varepsilon_0 = (\Phi_0/4\pi\lambda^2)$ denotes the vortex line energy and λ is the magnetic penetration depth. This approximation has been widely used in the context of vortex physics, see, e.g., Refs. [35–38]; it applies to situations, where vortex displacements, for instance due to a pinning defect or thermal fluctuations, remain small on the intervortex distance. In the limit where the other vortices, and hence the cage, remain fixed, the addition of $U_{\mathrm{cage}}(r)$ to $U_{\mathrm{tilt}}(r)$ then contributes the (constant) curvature $\pi\varepsilon_0/a_0^2$ to the Hessian. However, in general one may expect that the other vortices move as well when our test vortex observed in the experiment is moving, e.g., the depinning of the test vortex may induce avalanches in the surrounding vortex system. While this opens interesting questions deserving further studies, this setting is quite far away from our original question and we do not further pursue it here.

IV. HESSIAN CHARACTER OF PINSCAPES

We now turn to the main part of this paper, the calculation of the Hessian character $\mathcal{C}_{\mathrm{pos}}$ of a pinscape. This number quantifies the fraction (less than unity) of the plane's area that admits a stable vortex position (i.e., a positive definite Hessian matrix) under an appropriate tilt force. The Hessian has been used in the characterization of various functions in a multitude of fields, including optics [29,30], statistical physics of random systems [27,28,31], or cosmology [39], see Ref. [28] for a more detailed list of references. Those studies typically focus on a set of specific critical points in a given

area (corresponding to extremal points at a given fixed tilt in the present context), while we aim at characterizing every point in space as potentially giving rise to a minimum under an appropriate tilt. As a result, here, we determine the area fractions with specific curvature properties.

A point $\boldsymbol{r}\in\Omega$ in the two-dimensional landscape of area Ω is called stable if the local potential landscape features a positive-definite Hessian matrix; the collection of such stable positions defines the stability regions of the pinscape where the pinscape can be mapped through the spectroscopic method described in Sec. II.

A. Single defect

As a warmup, consider the pinscape of a single defect. Here, we focus on isotropic defects with a potential $V(\boldsymbol{r}) = V(r)$, assuming a minimum $-V_0$ at the origin $r = 0$, and a monotonic radial dependence $V'(r) > 0$, where the prime $'$ denotes the radial derivative $V'(r) = \partial_r V(r)$. We demand the potential to be integrable, $\int d^2r\,|V(\boldsymbol{r})| < \infty$, implying its asymptotic decay $V(r\to\infty) = 0$; a notable exception is the long-range Lorentzian potential discussed below. The Hessian matrix of such an isolated defect possesses the eigenvalues $V''(r)$ and $V'(r)/r$; they describe longitudinal (along $\boldsymbol{r}$) and transverse (to $\boldsymbol{r}$) curvatures. While the latter is positive everywhere, the longitudinal curvature assumes a positive value only in the vicinity of the defect's center. Defining the stability radius ξ_0 through the condition $V''(r = \xi_0) = 0$, we find the stable area $\Omega_0 = \pi\xi_0^2$; at distances larger than ξ_0, the landscape is indefinite. Maxima appear in the pinscape only through the interference of (at least two) defects.

For the specific cases of a Gaussian-shaped

$$V_{\rm G}(r) = -V_0\exp(-r^2/\xi^2) + \bar{V}_{\rm G} \tag{16}$$

and Lorentzian-shaped

$$V_{\rm L}(r) = -V_0/(1 + r^2/\xi^2) + \bar{V}_{\rm L} \tag{17}$$

defect potential, we find the stability radii $\xi_0 = \xi/\sqrt{2}$ and $\xi_0 = \xi/\sqrt{3}$, respectively. The constant shifts $\bar{V}_{\rm G} = V_0\pi\xi^2/\Omega$ and $\bar{V}_{\rm L} = V_0(\pi\xi^2/\Omega)\ln[1 + (\Omega/\pi\xi^2)]$ assure a vanishing potential average, i.e., $\int_\Omega d^2r\,V(\boldsymbol{r}) = 0$. Below, we will also consider the case of a cut parabola

$$V_{\rm P}(r) = -V_0(1 - r^2/\xi^2)\Theta(r - \xi) + \bar{V}_{\rm P}, \tag{18}$$

with $\xi_0 = \xi$ and $\bar{V}_{\rm P} = V_0\pi\xi^2/2\Omega$; this type of potential has often been used in numerical simulations of vortex pinning [21,22].

Next, we consider a pinscape originating from a small density $n_p = N/\Omega$ of defects, where N denotes the number of defects in the area Ω. For a very low density of defects, $n_p\Omega_0 \ll 1$, the probability $\sim(n_p\xi^2)^2$ for defects to overlap is parametrically small; as a result the stability region to leading order in $n_p\xi^2$ assumes the value

$$\mathcal{C}_{\rm pos} \approx n_p\Omega_0. \tag{19}$$

This generic result tells, that only a minute areal fraction in the immediate vicinity of defects is capable of being probed within the vortex-in-a-maze scheme.

B. Gaussian limit of dense defects

The nontrivial and hence interesting structure of a pinscape develops when defect potentials start to overlap. Below, we study pinning landscapes of the type

$$U(\boldsymbol{r}) = \sum_{j=1}^{N} V(\boldsymbol{r} - \boldsymbol{r}_j). \tag{20}$$

We assume $\int_\Omega d^2r\,V(\boldsymbol{r}) = 0$ such that the potential U averages to zero as well. Given a random distribution of defect positions $\boldsymbol{r}_j$, the pinscape turns into a random energy surface. Our task now consists in determining the (mean) character $\mathcal{C}_{\rm pos}$ for specific types of random landscapes. The latter is defined through the probability density $p(\mathfrak{D}, \mathfrak{T})$ of finding a position with given Hessian determinant $\det H = \mathfrak{D}$ and trace $\mathrm{tr}H = \mathfrak{T}$, both of which have to be positive $\mathfrak{D} > 0$ and $\mathfrak{T} > 0$,

$$\mathcal{C}_{\rm pos} = \int_0^\infty\!\!\int_0^\infty d\mathfrak{D}\,d\mathfrak{T}\;p(\mathfrak{D}, \mathfrak{T}). \tag{21}$$

Characterizing the random pinscape potential $U(\boldsymbol{r})$ through its functional probability measure $\mathcal{P}[U(\boldsymbol{r})]$, we find the probability density $p(\mathfrak{D}, \mathfrak{T})$ via functional integration,

$$p(\mathfrak{D}, \mathfrak{T}) = \int \mathcal{D}[U(\boldsymbol{r})]\,\mathcal{P}[U(\boldsymbol{r})]\,\delta[\det H - \mathfrak{D}]\,\delta[\mathrm{tr}H - \mathfrak{T}], \tag{22}$$

where the Hessian matrix H can be evaluated at any spatial point $\boldsymbol{r}$ due to the translation invariance of the result; without loss of generality, we choose $\boldsymbol{r} = \boldsymbol{0}$. For a homogeneous distribution of N defects in an area Ω, see Eq. (20), the measure in (22) is given by

$$\mathcal{D}[U(\boldsymbol{r})]\,\mathcal{P}[U(\boldsymbol{r})] = \prod_{j=1}^{N}\left[\frac{d^2r_j}{\Omega}\right]. \tag{23}$$

A second generic result [besides the trivial dilute limit (19)] can then be obtained in the high density limit $n_p\Omega_0 \gg 1$ when many defects overlap. As shown in Appendix D, the pinscape of many overlapping defects approaches a Gaussian distribution with vanishing mean $\langle U(\boldsymbol{r})\rangle = 0$ [since $\langle V(\boldsymbol{r})\rangle = 0$] and a two-point correlator

$$G(\boldsymbol{r} - \boldsymbol{r}') = \langle U(\boldsymbol{r})U(\boldsymbol{r}')\rangle = n_p\int d^2s\,V(\boldsymbol{r} - \boldsymbol{s})V(\boldsymbol{r}' - \boldsymbol{s}) \tag{24}$$

deriving from the convolution of two shifted potentials $V(\boldsymbol{r})$. It follows from the central limit theorem that the distribution function $\mathcal{P}[U(0)]$ for the potential in a fixed point, e.g., at the origin, is of Gaussian form. The fact that the *functional* distribution function $\mathcal{P}[U(\boldsymbol{r})]$ becomes Gaussian as well,

$$\mathcal{P}[U(\boldsymbol{r})] = \mathcal{P}_{\rm G}[U(\boldsymbol{r})] = e^{-\mathcal{S}}/\mathcal{Z}, \tag{25}$$

with $\mathcal{Z} = \int \mathcal{D}[U(\boldsymbol{r})]\,e^{-\mathcal{S}}$ and the quadratic action

$$\mathcal{S} = \frac{1}{2}\int\frac{d^2r}{\Omega}\int\frac{d^2r'}{\Omega}\,U(\boldsymbol{r})\,G^{-1}(\boldsymbol{r} - \boldsymbol{r}')\,U(\boldsymbol{r}'), \tag{26}$$

is less trivial and can be checked by confirming the validity of Wick's theorem for the $2k$-point correlators (up to corrections in the small parameter $1/n_p\Omega_0$) or via a direct calculation of $\mathcal{P}[U(\boldsymbol{r})]$, see Appendix D.

For such a Gaussian random potential, symmetry imposes that regions of positive- and negative-definite Hessians (i.e., with $\mathfrak{D}>0$ and $\mathrm{sign}(\mathfrak{T})=\pm 1$ respectively) are equally probable and hence Eq. (21) reduces to the evaluation of the simpler expression

$$\mathcal{C}_{\rm pos} = \frac{1}{2}\int_0^\infty d\mathfrak{D}\; p(\mathfrak{D}), \tag{27}$$

where $p(\mathfrak{D})$ denotes the probability distribution of the Hessian determinant $\det H$ taking the value $\mathfrak{D}$.

The task of finding the probability density $p(\mathfrak{D})$ can be broken up into a sequence of problems: In a first step, we can determine the probability $\pi(a,b,c)$ for a Hessian matrix to assume diagonal entries $2a$, $2b$ and off-diagonal entries c, thereby reducing the problem of evaluating Eq. (27) to an algebraic integral,

$$p(\mathfrak{D}) = \int da\, db\, dc\, \pi(a,b,c)\, \delta[4ab - c^2 - \mathfrak{D}]. \tag{28}$$

We find the probability function $\pi(a,b,c)$ via the functional integration

$$\pi(a,b,c) = \int \mathcal{D}[U(\boldsymbol{r})]\, \mathcal{P}_{\rm G}[U(\boldsymbol{r})]\, 4\, \delta[U_{xx}(0) - 2a] \times \delta[U_{yy}(0) - 2b]\, \delta[U_{xy}(0) - c]. \tag{29}$$

The numerical factor 4 appears from applying the identity $\delta[U_{xx}(0)/2 - a] = 2\,\delta[U_{xx}(0) - 2a]$ and equally for $\delta[U_{yy}(0)/2 - b]$. The difficulty with the functional integration over all realizations $U(\boldsymbol{r})$ is now moved to the evaluation of $\pi(a,b,c)$ in Eq. (29).

Substituting Eq. (26) into Eq. (29) and expressing the δ distributions in Fourier space, we have to the evaluate

$$\pi(a,b,c) = \frac{1}{\mathcal{Z}}\int \mathcal{D}[U(\boldsymbol{r})] e^{-\frac{1}{2}\int\frac{d^2r}{\Omega}\int\frac{d^2r'}{\Omega}U(\boldsymbol{r})G^{-1}(\boldsymbol{r}-\boldsymbol{r}')U(\boldsymbol{r}')} \times \int \frac{dk\, dl\, dm}{(2\pi)^3} 4 e^{i(2ka+2lb+mc)} \times e^{-i\int d^2r[kU_{xx}(\boldsymbol{r})+lU_{yy}(\boldsymbol{r})+mU_{xy}(\boldsymbol{r})]\delta(\boldsymbol{r})}. \tag{30}$$

Two integrations by parts in the exponent of the last factor yield $\int d^2r\, U(\boldsymbol{r})[k\delta_{xx}(\boldsymbol{r}) + l\delta_{yy}(\boldsymbol{r}) + m\delta_{xy}(\boldsymbol{r})]$, with $\delta_{\kappa\mu}(\boldsymbol{r}) \equiv \partial^2\delta(\boldsymbol{r})/\partial x_\kappa \partial x_\mu$. The remaining functional integration can now be performed through Gaussian integration [40,41] (i.e., completing the square),

$$\pi(a,b,c) = \int \frac{dk\, dl\, dm}{(2\pi)^3} 4 e^{i(2ka+2lb+mc)} \times e^{-\frac{1}{2}[k^2 G_0^{xxxx} + l^2 G_0^{yyyy} + (m^2+2kl) G_0^{xxyy}]}, \tag{31}$$

where $G_0^{\kappa\mu\nu\sigma} \equiv \partial^4 G(\boldsymbol{r})/\partial x_\kappa \partial x_\mu \partial x_\nu \partial x_\sigma|_{\boldsymbol{r}=0} > 0$ denotes the fourth derivative of the Green's function. For an isotropic problem, symmetry tells that $G_0^{(4)} \equiv G_0^{xxyy} = G_0^{xxxx}/3 = G_0^{yyyy}/3$ and hence

$$\pi(a,b,c) = \int \frac{dk\, dl\, dm}{(2\pi)^3} 4 e^{i(2ka+2lb+mc)} \times e^{-\frac{1}{2}[3k^2 G_0^{(4)} + 3l^2 G_0^{(4)} + (m^2+2kl) G_0^{(4)}]}. \tag{32}$$

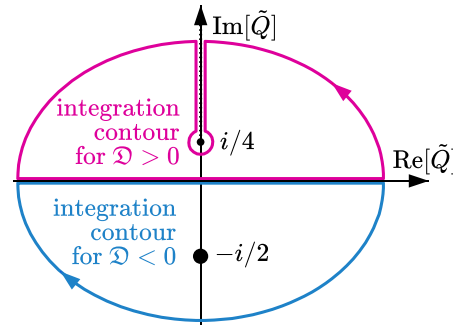

FIG. 3. Sketches of the contours in the complex plane for evaluating integral in Eq. (35). For $\mathfrak{D}>0$, the (magenta) contour encloses the upper half-plane except for the cut along the imaginary axis starting from $i/4$. For $\mathfrak{D}<0$, the (blue) contour encloses the lower half-plane with a pole at $-i/2$.

The remaining Gaussian integrations over k, l, and m then yield the result

$$\pi(a,b,c) = \frac{4 e^{-(3a^2-2ab+3b^2+2c^2)/4G_0^{(4)}}}{\left(4\pi G_0^{(4)}\right)^{3/2}} \tag{33}$$

and we find that the probability distribution of Hessian matrix elements is Gaussian, as one might have expected for a Gaussian distributed random potential.

Making use of the result (33) in Eq. (28), we find the distribution

$$p(\mathfrak{D}) = \frac{4}{\left[4\pi G_0^{(4)}\right]^{3/2}}\int\frac{dQ}{2\pi}\int da\, db\, dc\, e^{iQ\mathfrak{D}} \times e^{-iQ(4ab-c^2)} e^{-(3a^2-2ab+3b^2+2c^2)/4G_0^{(4)}}, \tag{34}$$

which after another series of Gaussian integrations gives

$$p(\mathfrak{D}) = \int_{-\infty}^{\infty}\frac{d\tilde{Q}}{2\pi G_0^{(4)}}\frac{e^{i\tilde{Q}\mathfrak{D}/G_0^{(4)}}}{\sqrt{(1-2i\tilde{Q})^2(1+4i\tilde{Q})}}, \tag{35}$$

with $\tilde{Q} = QG_0^{(4)}$. The integrand has a pole of order one in the negative complex plane at $\tilde{Q} = -i/2$ and a line cut along the positive imaginary axis, terminating at $\tilde{Q} = i/4$, see Fig. 3. The above integral can be solved for $\mathfrak{D}>0$ using a closed contour in the upper complex plane avoiding the line cut along the imaginary axis. We then find with the substitution $\zeta = \mathrm{arccot}[(4q/3)^{1/2}]$

$$p(\mathfrak{D}>0) = \frac{2e^{-\mathfrak{D}/4G_0^{(4)}}}{G_0^{(4)}}\int_0^\infty\frac{dq}{2\pi}\frac{e^{-q\mathfrak{D}/G_0^{(4)}}}{(3+4q)\sqrt{q}} \tag{36}$$

$$= \frac{2e^{\mathfrak{D}/2G_0^{(4)}}}{\sqrt{3}G_0^{(4)}}\int_0^{\pi/2}\frac{d\zeta}{2\pi}e^{-\left(3\mathfrak{D}/4G_0^{(4)}\right)(\sin\zeta)^{-2}}. \tag{37}$$

The integral in the last line is Craig's formula [42] for the complementary error function $\mathrm{erfc}[z] \equiv 1 - \mathrm{erf}[z]$ for nonnegative $z = (3\mathfrak{D}/4G_0^{(4)})^{1/2}$, with the error function defined as $\mathrm{erf}(z) = (4/\pi)^{1/2}\int_0^z dt\, e^{-t^2}$. For $\mathfrak{D}<0$ the contour is closed in the lower half-plane, encircling the pole at $\tilde{Q} = -i/2$. The residue theorem then yields $p(\mathfrak{D}<0) = e^{\mathfrak{D}/2G_0^{(4)}}/(2\sqrt{3}G_0^{(4)})$. The probability distribution $p(\mathfrak{D})$ for the Hessian determinant

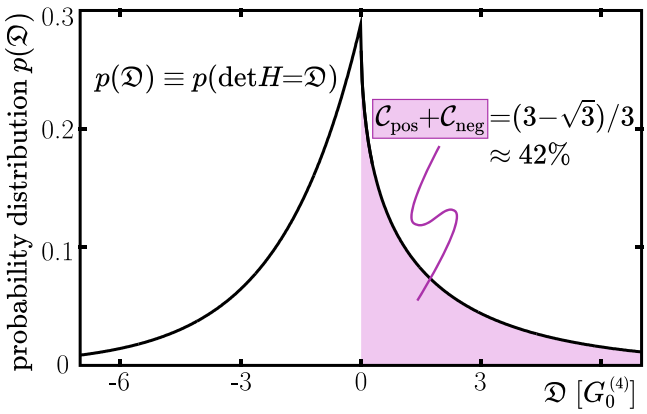

FIG. 4. Probability distribution function $p(\mathfrak{D})$ of the Hessian $\det H$ for a Gaussian distributed random potential, see Eq. (38). The horizontal axis measures the determinant $\mathfrak{D}$ in units of $G_0^{(4)}$. The shaded probability indicates the area-fraction of points with positive- or negative-definite curvature.

then takes the compact global form (see Fig. 4 for an illustration)

$$p(\mathfrak{D}) = \frac{e^{\mathfrak{D}/2G_0^{(4)}}}{2\sqrt{3}G_0^{(4)}}\left[1-\mathrm{erf}\left(\sqrt{\frac{3}{4}\frac{\mathfrak{D}}{G_0^{(4)}}}\right)\Theta\left(\mathfrak{D}/G_0^{(4)}\right)\right], \qquad (38)$$

where we have expressed the result through the Heaviside function $\Theta(z)=1$ for $z>0$ (and zero otherwise). The result behaves as $p(\mathfrak{D})\approx p(0)[1-(3\mathfrak{D}/\pi G_0^{(4)})^{1/2}]$ at small positive arguments $0<\mathfrak{D}/G_0^{(4)}\ll 1$ and decays exponentially with $p(\mathfrak{D}) \approx p(0)(4G_0^{(4)}/3\pi\mathfrak{D})^{1/2}\exp(-\mathfrak{D}/4G_0^{(4)})$ for large values $\mathfrak{D}/G_0^{(4)} \gg 1$.

With the full expression for $p(\mathfrak{D})$ at hand, the stable area fraction $\mathcal{C}_{\rm pos}$ of the two-dimensional (Gaussian-distributed) potential landscape can be determined: It is convenient to use the expression (36) and integrate over $\mathfrak{D}$ first; the subsequent integral over q then yields the universal result

$$\mathcal{C}_{\rm pos} = (3-\sqrt{3})/6 \approx 0.21, \qquad (39)$$

independent of $G_0^{(4)}$ and thus of the shape of the correlator. We find that for a Gaussian random potential the stable area involves about one-fifth of the total landscape; in physical terms it means that only a small fraction the landscape can be explored by pinscape spectroscopy, while a large portion (nearly 80%) of the plane are either unstable or indefinite areas.

C. Intermediate defect densities

At intermediate densities, we have to resort to numerical studies; these will provide us—besides the desired information on the stable fraction $\mathcal{C}_{\rm pos}$—with some additional insights on the fraction of unstable ($\mathcal{C}_{\rm neg}$) and indefinite regions ($\mathcal{C}_{\rm ind}$) of such random landscapes.

We have explored this regime for the three different types of defect potentials, cut parabolas $V_{\rm P}(r)$, Lorentzian-shaped $V_{\rm L}(r)$ with algebraic tails, and short-range Gaussian-shaped $V_{\rm G}(r)$, and computed the area fractions $\mathcal{C}_{\rm pos}$, $\mathcal{C}_{\rm neg}$, and $\mathcal{C}_{\rm ind}$ for stable, negative-definite and indefinite regions, respectively. This numerical analysis reveals several interesting facts, see

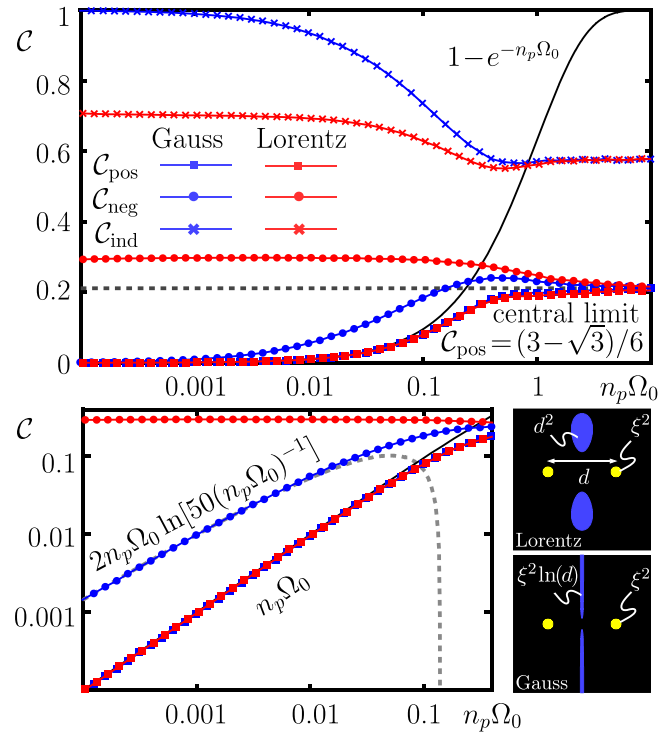

FIG. 5. Fraction of stable ($\mathcal{C}_{\rm pos}$, squares), unstable ($\mathcal{C}_{\rm neg}$, circles), and indefinite ($\mathcal{C}_{\rm ind}$, crosses) areas of a potential landscape characterized by a finite density n_p of Lorentzian [$V_{\rm L}(r)$, red] or Gaussian [$V_{\rm G}(r)$, blue] shaped defects potentials, respectively. The log-linear scale (top) highlights the behavior at large densities, while the scaling at low densities is more prominent in the log-log representation (bottom). At small densities the fraction of stable points follows the universal law $\mathcal{C}_{\rm pos} = n_p\Omega_0$, see bottom figure. At large densities the Hessian character approaches that of a random potential with Gaussian correlator (black dashed line in top panel). The stable area fraction of the cut parabolic trap $V_{\rm L}(r)$ is shown as a black line in the top panel. At low defect densities $n_p\Omega_0 \to 0$, see bottom panel, the unstable fraction $\mathcal{C}_{\rm neg}$ reaches a constant value for the Lorentzian-shaped potential (red circles) and decays as $\mathcal{C}_{\rm neg} \sim n_p\Omega_0\ln[(n_p\Omega_0)^{-1}]$ for the Gaussian-shaped potential (blue circles). This is owed to the different scaling of unstable regions defined by distant defects in the dilute limit, as shown in the two thumbnails on the bottom right with yellow (stable), blue (unstable/maxima), and black (unstable/saddle points) areas.

Fig. 5: First, the Hessian character $\mathcal{C}_{\rm pos}$ grows linearly from zero (at low densities). For the regular potentials $V_{\rm L}(r)$ and $V_{\rm G}(r)$, the stable fraction saturates rapidly (i.e., for $n_p\Omega_0 \gtrsim 4$) to the value obtained for a Gaussian random pinscape, with the precise functional dependence on the density parameter $n_p\Omega_0$ differing numerically. The (irregular) cut parabolas $V_{\rm P}(r)$, however, behave differently, with the entire area becoming stable at large densities n_p, $\mathcal{C}_{\rm pos} \to 1$, see below for more details.

A qualitative difference is observed between $V_{\rm L}$ and $V_{\rm G}$ for the negative-definite area-fraction $\mathcal{C}_{\rm neg}$ (the latter vanishes identically for $V_{\rm P}$). This quantity assumes a macroscopic value $\sim$30% for the long-range Lorentzian traps, while vanishing at low densities for the Gaussian-shaped pins, see Fig. 5 (bottom). The difference is attributed to the long-range, i.e.,

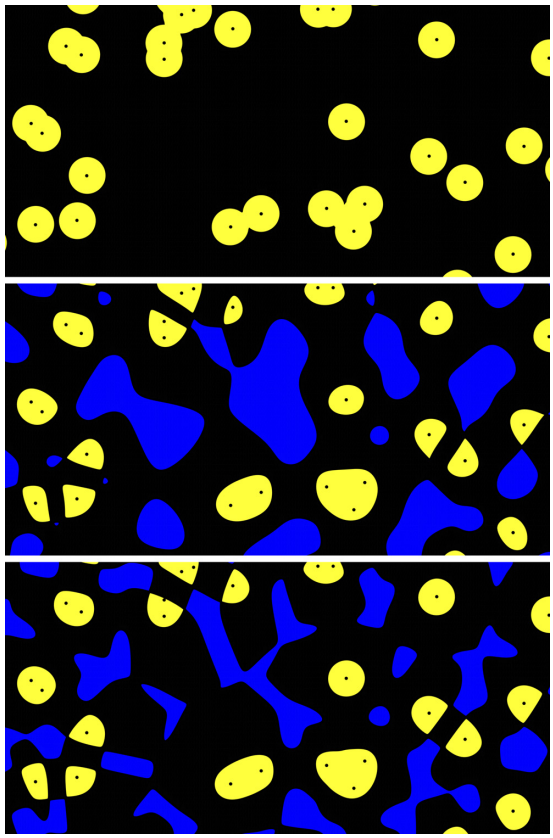

FIG. 6. Hessian map of a potential landscape for a moderate density of cut parabolic (top), Lorentzian (middle), and Gaussian (bottom) traps. To allow for direct comparison, the defect position is the same in all panels (we chose a density parameter $n_p\xi_G^2 = 0.125$ and the view area $100\,\xi_G \times 50\,\xi_G$) and the length ξ (defining the defect shape) assumes the values $(1/2)^{1/2}\xi_G$, $(3/2)^{1/2}\xi_G$, and ξ_G respectively. This implies an elementary area fraction of $n_p\Omega_0 \approx 0.2$ for all three cases. Yellow/blue denote stable/unstable regions where the Hessian matrix is positive/negative definite. Indefinite points are colored in black. Here, the difference in the area fraction $\mathcal{C}_{\rm neg}$ of unstable points for the Lorentzian (∼28%) and Gaussian (∼22%) traps is apparent, see Fig. 5.

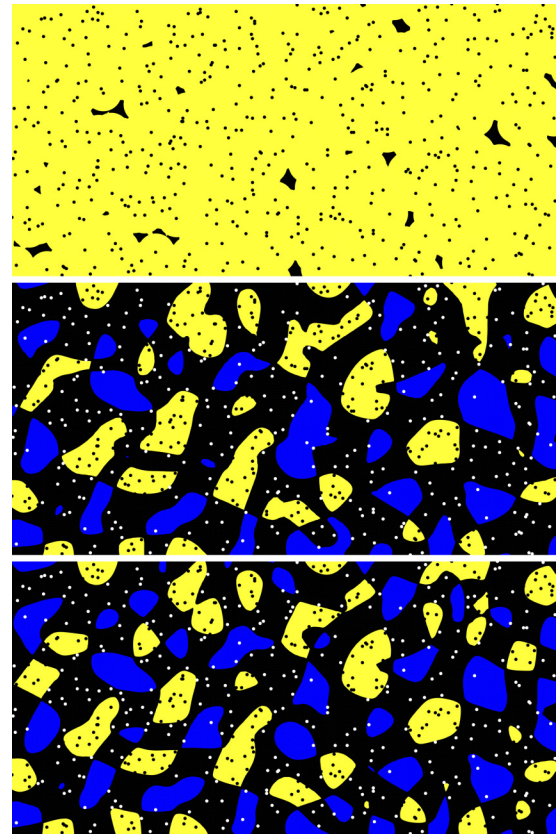

FIG. 7. Hessian map of a potential landscape for a high density of cut parabolas (top), Lorentzian (middle), and Gaussian (bottom) traps. The defect position is equal in all panels (we chose a density parameter $n_p\xi_G^2 = 2.5$ and a view area $100\,\xi_G \times 50\,\xi_G$). The length parameter ξ (defining the defect shape) assumes the values $(1/2)^{1/2}\xi_G$, $(3/2)^{1/2}\xi_G$, and ξ_G respectively. The elementary area fraction is $n_p\Omega_0 \approx 4$. Yellow/blue denotes stable/unstable regions where the Hessian matrix is positive/negative definite. Indefinite points are black. Dense defect clusters (black points in yellow domains) define stable pinning regions, low density areas (white defects in blue regions) are unstable.

power-law, nature of the potential and can be understood by considering a pair of defects: For a single (rotationally symmetric) defect, the transverse curvature (along the azimuth) is always positive, while the longitudinal curvature (along the radius) changes from positive near the center to negative further out. Hence, a single defect generates either minima or saddles and a pair of defects is required to produce a maximum through proper superposition of the two negative longitudinal curvatures.

For a pair of defects with long-ranged potential (e.g., Lorentzian) at a distance d, the decay of the tails $[V(r) \sim r^{-\alpha},\ \alpha > 1]$ has no intrinsic length scale, and the area of regions with negative curvature scales as d^2. This area becomes anisotropic [width × height $\approx (d/\sqrt{\alpha}) \times (\sqrt{\alpha}d)$, see thumbnail in Fig. 5] as α increases. At low defect density, the height $\sqrt{\alpha}d$ gets cut off by the typical inter-defect distance $d = n_p^{-1/2}$, resulting in a concave area $\propto d^2/\sqrt{\alpha}$. The area fraction $\mathcal{C}_{\rm neg} \propto (n_p\Omega_0)^0/\sqrt{\alpha}$ with negative curvature is nonvanishing in the limit $n_p \to 0$. For short-ranged defects, i.e., where a length-scale ξ dictates the decay away from the defect, the result is not universal as it depends on the negatively curved overlap produced by two distant defects. Specifically, for two defects separated by d, the negative overlap is limited to a slim area concentrated near the normal (line) to the midpoint between the defects (Wigner-Seitz or Voronoi decomposition), see thumbnails in Fig. 5. For Gaussian-shaped defect potentials, the area fraction can be evaluated to $(\xi/d)^2 \ln(d/\xi)$, yielding $\mathcal{C}_{\rm neg} \propto n_p\Omega_0 \ln[(n_p\Omega_0)^{-1}]$.

The special case of cut parabolas $V_{\rm P}(r)$ can be treated analytically, since curvatures are non-negative integer multiples of $2V_0/\xi^2$. More specifically, within a defect's range of action $r < \xi$, the Hessian matrix $H = (2V_0/\xi^2)\mathbb{I}$ is position independent, diagonal, and positive definite, while it vanishes outside. As a result, nonoverlapping traps act as isolated ones, while the total Hessian determinant of ν overlapping traps is $\nu^2(2V_0/\xi^2)^2 \geqslant 0$. We thus conclude that the only nonstable (and hence indefinite) regions are those where no

defect is active, i.e., where $\nu = 0$. This probability is given by the zeroth term of the Poisson distribution $\mathrm{Poiss}(\nu, n_p\Omega_0) = (n_p\Omega_0)^\nu \exp(-n_p\Omega_0)/\nu!$ (see Appendix E for a detailed discussion) and hence the complement defines the stable area,

$$\mathcal{C}_{\mathrm{pos}} = 1 - \mathrm{Poiss}(0, n_p\Omega_0). \tag{40}$$

This area fraction approaches unity at large defect densities n_p, see black line in Fig. 5 and top panel in Fig. 7, quite different from the other two examples of Gaussian and Lorentzian shaped potentials that approach the Gaussian limit $\mathcal{C}_{\mathrm{pos}} \approx 21\%$. This is due to the singular property of the cut parabola that does not provide any region with a negative definite Hessian; when the parabolas are cut rather than smoothly connected to zero, only convex and flat regions appear in the pinning potential landscape. This implies that results of vortex simulations carried out with cut parabolas (e.g., in Ref. [21]) have to be considered with some care, particularly at large defect densities.

Figures 6 and 7 illustrate our findings for the two cases of low, $n_p\Omega_0 = 1/5$, and high density parameters $n_p\Omega_0 = 4$, respectively. In Fig. 6, we show the Hessian map for a moderate density of cut parabolic (top), Lorentzian (middle), and Gaussian (bottom) defects. For the cut parabolas, the Hessian determinant assumes only discrete values that follow from the number of overlapping defects. While the shape of stable regions (yellow) are trivial for the cut parabolas, this is no longer the case for the Lorentzian/Gaussian potentials. In Fig. 7, we show the Hessian map for a large density of cut parabolic (top), Lorentzian (middle), and Gaussian (bottom) defects. For the cut parabolas, the Hessian determinant guarantees stability in almost every point on the map. For the smooth Lorentzian and Gaussian potentials, different pins mutually neutralize one another and the stable regions are more scarce. Only when defects cluster, they reinforce one another to produce stable regions, see black dots in yellow regions. On the contrary, dilute regions with fewer defects than average (white dots in blue domains) produce unstable regions.

V. SUMMARY AND CONCLUSION

Inspired by the recent advances in vortex imaging and the development of pinscape spectroscopy, we have analyzed the properties of 2D pinning landscapes with the help of a new characteristics, the Hessian matrix $H(\boldsymbol{r})$, its determinant $\det H$, and its trace $\mathrm{tr}H$. We have introduced the *Hessian stability map* as a bicolored map that separates stable from unstable regions of the pinscape; while stable regions can be mapped via pinscape spectroscopy using appropriate (linear) driving forces, unstable regions cannot, i.e., these regions do not provide equilibrated vortex positions for any applied (linear) force. We have drawn attention to several peculiarities of pinscape spectroscopy (the so-called "spring-softening" and "broken-spring" effects in Ref. [9]) related to the stability boundaries of the Hessian map where the determinant $\det H$ vanishes, e.g., an enhanced response involving potential nonlinearities as well as the thermal activation over barriers into the unstable regions. Furthermore, we have indicated how pinscape spectroscopy can be enhanced to cover extended regions around the vortex trajectories by probing the out-of-phase response of vortices at high frequencies.

Second, we have introduced the *Hessian character* $\mathcal{C}_{\mathrm{pos}}$ of a pinning landscape $U(\boldsymbol{r})$ as the area fraction of the plane that covers the stable regions of the Hessian map. We have investigated two types of generic pinscapes, those arising from a random distribution of defects with individual pinning potentials $V(\boldsymbol{r})$ and the case of a Gaussian random potential characterized through its correlator $G(\boldsymbol{r})$. Different individual defect potentials $V(\boldsymbol{r})$ have been studied, cut parabolas with a discrete Hessian map and an exceptionally large stable fraction $\mathcal{C}_{\mathrm{pos}} \to 1$ at large defect densities $n_p\Omega_0 \gg 1$, Lorentzian-shaped trapping potentials that induce correlations through their long-range tails and produce a finite unstable fraction $\mathcal{C}_{\mathrm{neg}}$ in the limit of small defect density $n_p\Omega_0 \ll 1$, and Gaussian shaped potentials with a short range that behave most regularly at all densities—we infer that this type of pinning potential is suited best for numerical simulations of pinned vortex matter. The Hessian character of both, Gaussian and Lorentzian potentials, approaches the character of the random Gaussian potential for large defect densities $n_p\Omega_0 \gg 1$, with the latter assuming a universal value of $\mathcal{C}_{\mathrm{pos}} \approx 21\,\%$ independent of the correlator $G(\boldsymbol{r})$. Hence, we find that pinscape spectroscopy of regular pinning potentials can probe at most a fraction of about one-fifth of the plane.

Up to now, the vortex-in-a-maze experiment is limited to a single tunable drive parameter. This is owed to the experimental setup measuring the vortex motion in the region of a current-driven strip. An expanded view on the pinscape within this setup can be gained by injecting the vortex at different positions along the transverse ($\hat{\boldsymbol{y}}$) direction. However, other geometries allowing for different drive directions may open the possibility to probe the full stable region of a pinscape, thus coming closer to the original ball-in-a-maze setup also for the vortex.

The usefulness of the Hessian stability analysis for understanding vortex pinning cannot be overestimated: In the present paper, our focus has been mainly on mesoscopic vortex physics, where we provide a better understanding of the pinning landscape and its dependence on defect densities and potential shapes. As we have shown, these insights are of much help in analyzing data on vortex imaging [9]. With a view on numerical simulations, our study separates the "irregular" cut-parabolic [with a nonstandard high-density limit $\mathcal{C}_{\mathrm{pos}}(n_p\Omega_0 \gg 1) \to 1$] and Lorentzian potential shapes [with a nonstandard low-density limit $\mathcal{C}_{\mathrm{neg}}(n_p\Omega_0 \to 0) \to \mathrm{const.}$] from the "bread and butter" Gaussian shape that is regular at all densities and thus potentially better suitable for vortex simulations in a disordered environment.

Furthermore, the Hessian analysis is relevant in macroscopic vortex physics, e.g., transport in the context of strong pinning theory [43–45]. Indeed, the tilted random potential $U_{\mathrm{tilt}}(\boldsymbol{r}, F_{\mathrm{L}})$ serving as the starting point of our analysis can be directly mapped to the strong pinning problem in the single-vortex–single-pin setup: Within the strong pinning paradigm, the many-body problem of vortex lattice pinning is reduced to the minimization of the two-dimensional total pinning energy $e_{\mathrm{pin}}(\boldsymbol{r}) = \bar{C}(\boldsymbol{r} - \boldsymbol{x})^2/2 + V(\boldsymbol{r})$ including both an elastic energy (with $\bar{C}$ an effective elastic constant) and the pinning potential $V(\boldsymbol{r})$ of an individual defect. Under strong pinning conditions with $V(\boldsymbol{r})$ dominating the elastic term, the position $\boldsymbol{r}$ of the pinned vortex undergoes pinning and depinning jumps

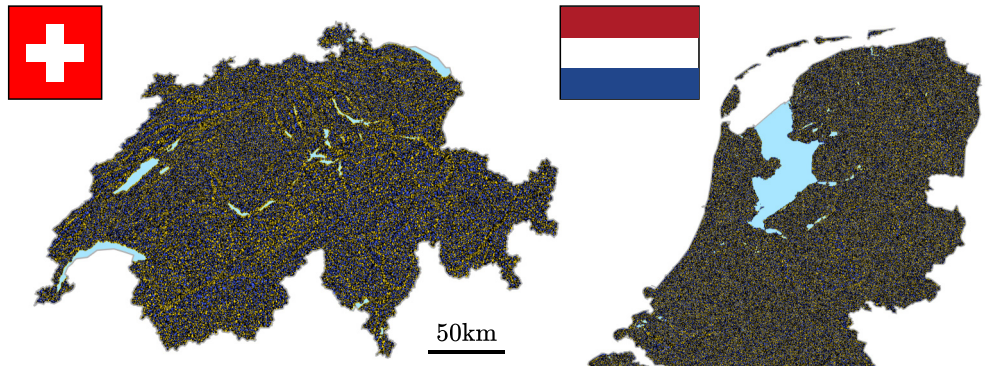

		Switzerland	Netherlands	Gauss. rand. pot.
$\mathcal{C}_{\rm pos}$		20.7%	20.5%	21.1%
$\mathcal{C}_{\rm neg}$		19.2%	18.9%	21.1%
$\mathcal{C}_{\rm ind}$		60.1%	60.6%	57.8%

FIG. 8. Hessian map of two natural landscapes: For Switzerland (left) and the Netherlands (right) stable, unstable, and indefinite areas are colored in yellow, blue, and black respectively. From an elevation map on a square lattice with longitude and latitude angular resolution of 15 arcseconds (data from Wolfram Mathematica's geographic data package), the Hessian matrix is evaluated by fitting a quadratic polynomial through each 3×3 plaquette. Despite the two countries having very different topography, their Hessian characters—tabled above—are close to the Gaussian result $\mathcal{C}_{\rm pos} = \mathcal{C}_{\rm neg} \approx 21.1\%$, see Eq. (39).

as the lattice moves smoothly along $\hat{\boldsymbol{x}}$, similar to our vortex-in-a-maze that gets trapped and detrapped by stable regions of the pinscape. Indeed, expanding the total pinning energy $e_{\rm pin}(\boldsymbol{r}) = \bar{C}\,x^2/2 - \bar{C}\,\boldsymbol{r}\cdot\boldsymbol{x} + V_{\rm eff}(\boldsymbol{r})$ with the renormalized effective potential $V_{\rm eff}(\boldsymbol{r}) = V(\boldsymbol{r}) + \bar{C}\,r^2/2$ (the term $\bar{C}\,x^2/2$ is an irrelevant shift), we reduce the strong pinning problem to the vortex-in-a-maze problem with the elastic term $\bar{C}\,\boldsymbol{r}\cdot\boldsymbol{x}$ replacing the external drive $\boldsymbol{F}_{\rm L}\cdot\boldsymbol{r}$ due to the current-induced Lorentz force (incidentally, the lattice coordinate $\boldsymbol{x}$ in the strong-pinning setup is driven by the applied current density $\boldsymbol{j}$ as well). This equivalence opens up interesting avenues in the strong pinning problem [46], see also Refs. [47,48]. In particular, one can show [49] that the pinning force density at the onset of strong pinning gets modified when generalizing the theory from isotropic to anisotropic defects; this is due to the Hessian stability map developing very different geometric structures in this case.

Besides this relation to strong pinning, one might think of completely different applications of Hessian maps and characters, a quite obvious one that comes to mind being natural (topographic) landscapes. Indeed, analyzing the elevation map of different topographic landscapes—we chose Switzerland and the Netherlands as examples, see Fig. 8—one finds in both cases the characters $\mathcal{C}_{\rm pos} \approx 21\,\%$, $\mathcal{C}_{\rm neg} \approx 19\,\%$, and $\mathcal{C}_{\rm ind} \approx 60\,\%$, close to the value for the Gaussian random landscape. We checked the stability of these Hessian characters under changes in the map's resolution and different data smoothing procedures. Our results raise interesting questions about possible universality and Gaussianity of natural landscapes, that require further investigations, though.

ACKNOWLEDGMENTS

We wish to express our special thanks to Eli Zeldov for initiating and supporting this project, to Yonathan Anahory for providing experimental input, and to Gian Michele Graf, who helped us formulating and solving the path integral problem of the Hessian matrix. The authors acknowledge financial support of the Swiss National Science Foundation (SNSF) through the NCCR MaNEP. R.W. further acknowledges the support from the Pauli Center for Theoretical Studies at ETH Zurich through its scientific visitor program and the Heidelberger Akademie der Wissenschaften (WIN, 8. Teilprogramm).

APPENDIX A: PARAMETER $\eta\omega/U''$

We derive an estimate for the parameter $\eta\omega/U''$ governing the response $\boldsymbol{u}$. Typical values for this ratio are obtained from the estimate $E_{\rm pin} \sim (H_c^2/4\pi)\,\xi^2 d_s$ of the vortex core energy in a film of thickness d_s; here, $H_c = \Phi_0/2\sqrt{2}\pi\lambda\xi$ denotes the thermodynamic critical field and λ and ξ are the penetration depth and the coherence length, respectively. The coherence length provides an estimate for the typical spatial variation in the pinscape and hence $U'' \sim E_{\rm pin}/\xi^2$. The viscosity η follows from the Bardeen-Stephen [50] formula $\eta = \Phi_0^2 d_s/2\pi\xi^2\rho_n c^2$, with the flux quantum $\Phi_0 = hc/2e = 2.07\times10^{-7}\,\mathrm{G\,cm^2}$. Inserting the Drude expression $\rho_n = m/ne^2\tau$ for the normal state resistivity, where n is the electronic density and τ the electron relaxation (scattering) time, we find the ratio

$$\eta\omega/U'' \sim (n/n_s)\omega\tau \tag{A1}$$

with n_s the superfluid density. Assuming a value n/n_s of order unity, we find the parameter $\eta\omega/U''$ to be small in general. For example, in the experiment on Pb-films of Ref. [9], the parameters $\xi = 46\,\mathrm{nm}$, $\lambda \approx 90$ nm, and $d_s = 75\,\mathrm{nm}$ provide an estimate $E_{\rm pin}/\xi^2 \approx 7.5\times10^{-5}\,\mathrm{N/m}$. Assuming a normal state resistivity $\rho_n \approx 0.01\,\mu\Omega\,\mathrm{cm}$ for lead [51], we find that $\eta \approx 2.4\times10^{-13}\,\mathrm{Ns/m}$ and combining this estimate with the *ac* frequency $\omega = 13.3\,\mathrm{kHz}$ of the experiment, we arrive at

$\eta\omega \approx 3.2 \times 10^{-9}$ N/m, a value that is 3–4 orders of magnitude lower than typical curvatures U''.

APPENDIX B: 2D LOCAL RECONSTRUCTION OF PINSCAPE

The solution of the equation of motion (1) provides us with the expressions

$$\frac{u_x}{F_{ac}} = \frac{4b^2+\eta^2\omega^2}{2b(4ab-c^2)+2a\eta^2\omega^2+i\eta\omega[4b^2+c^2+\eta^2\omega^2]}, \quad \text{(B1)}$$

$$\frac{u_y}{F_{ac}} = \frac{-c(2b-i\eta\omega)}{2b(4ab-c^2)+2a\eta^2\omega^2+i\eta\omega[4b^2+c^2+\eta^2\omega^2]} \quad \text{(B2)}$$

for the displacements u_x and u_y. This result can be analyzed perturbatively in the small parameter $\eta\omega/U''$ and leads us to the simple expression Eq. (5) to lowest (0th) order. The expansion of Eqs. (B1) and (B2) to linear order in $\eta\omega/U''$ contributes the out-of-phase displacements δu_x, $\delta u_y \propto i(\eta\omega/U'')(F_{ac}/U'')$ that allow for the full local construction of the pinscape $U(x,y)$ in the vicinity of the vortex trajectory. Specifically, this out-of-phase response assumes the form

$$\frac{\delta u_x}{F_{ac}} = -i\eta\omega\frac{4b^2+c^2}{(4ab-c^2)^2}, \quad \frac{\delta u_y}{F_{ac}} = i\eta\omega\frac{2(a+b)c}{(4ab-c^2)^2} \quad \text{(B3)}$$

and can be measured independently from the in-phase displacements in Eq. (5). For a fixed drive amplitude F_{ac}, the independent measurement of the four quantities u_x, u_y, δu_x, and δu_y then allows to extract all the local curvatures a, b, and c from the experiment, see Eqs. (10)–(12), with $u = (u_x^2 + u_y^2)^{1/2}$. The additional independent relation $\eta\omega = F_{ac}\,|\delta u_x|/u^2$ with a constant left-hand side $\eta\omega$ serves as a check. The results (10)–(12) can be used to reconstruct the potential in the vicinity of the trajectory. We define the vector $\boldsymbol{\eta}_\perp \equiv (1, -u_x/u_y) = (1, 2b_n/c_n)$ perpendicular to the vortex trajectory and parametrize the positions $\boldsymbol{r}_{n,\epsilon} = \boldsymbol{r}_n + \epsilon\boldsymbol{\eta}_\perp$ transverse to the equilibrium trajectory at $\boldsymbol{r}_n$. Combining Eqs. (10)–(12) and (7), we find the potential shift

$$\begin{aligned} U(\boldsymbol{r}_{n,\epsilon}) - U(\boldsymbol{r}_n) &= \epsilon F_{Ln} + \epsilon^2\left[a_n + 2b_n + 4b_n^3/c_n^2\right] \\ &= \epsilon F_{Ln} + \epsilon^2\frac{F_{ac}}{2u_x}\left[1+\frac{u^2/u_y^2}{(\delta u_y/u_y)(u_x/\delta u_x)-1}\right]. \end{aligned} \quad \text{(B4)}$$

While the linear term $\propto \epsilon$ in the bare potential is "tilted away" by the force $F_{Ln} = nF_{ac}$, the quadratic term $\propto \epsilon^2$ provides the parabolic confinement transverse to the vortex trajectory. Unfortunately, the corrections Eq. (B3) are small in the parameter $\eta\omega/U''$, requiring a high measurement sensitivity and *ac* frequencies in the MHz range.

The solutions Eqs. (5) and (B3) for the in-phase and out-of-phase motion apply when $\delta u_x/u_x,\ \delta u_y/u_y \ll 1$, i.e., when

$$\eta\omega \ll \frac{2b(4ab-c^2)}{4b^2+c^2} \quad \text{and} \quad \eta\omega \ll \frac{4ab-c^2}{2(a+b)}. \quad \text{(B5)}$$

These criteria are violated in the vicinity of the *Hessian boundary* where the condition $4ab - c^2 = 0$ is separating a stable from an unstable region. Near this boundary, the singularities in Eq. (5) are cut off by the dissipative term $\eta\omega$ and the appropriate solutions to linear order in $F_{ac}/\eta\omega$ take the form

$$\frac{u_x}{F_{ac}} = \frac{-i}{\eta\omega}\frac{1}{1+(c/2b)^2}, \quad \frac{u_y}{F_{ac}} = \frac{i}{\eta\omega}\frac{c/2b}{1+(c/2b)^2}. \quad \text{(B6)}$$

These displacements are phase lagged with respect to the external drive, while the motion is still at the same angle ϕ away from the x axis.

APPENDIX C: ESCAPE

Here, we comment on the escape of the vortex from the stable region when approaching the Hessian boundary. The quadratic approximation (2) then is insufficient to describe the escape dynamics over the depinning barrier. The latter is obtained by including cubic terms in the expansion; limiting ourselves to the most relevant term $d\,u_x^3$, we obtain the expansion around the position $\boldsymbol{r}_0$ near the boundary

$$U_{\text{tilt}}(\boldsymbol{r}, F_{\text{L}}) = U_{\text{tilt}}(\boldsymbol{r}_0, F_{\text{L}}) + au_x^2 + bu_y^2 + cu_xu_y + du_x^3$$

with $d < 0$ describing the escape for positive tilt. This potential features a saddle point at

$$\boldsymbol{r} = \boldsymbol{r}_0 - \frac{2\tilde{a}}{3d}(1, -c/2b) \quad \text{(C1)}$$

and defines a barrier

$$U_b = 4\tilde{a}^3/27d^2 \quad \text{(C2)}$$

that prevents the escape of the vortex to the unstable region; here, we have introduced the renormalized curvature $\tilde{a} = a(1 - c^2/4ab)$, which scales linearly with the Hessian determinant and vanishes upon approaching the stability edge. Note that the curvature parameters in the above expressions depend on $\boldsymbol{r}_0$ and hence on the closeness of this point to the Hessian stability boundary.

At finite temperature, the vortex escapes the defect by thermal activation when the criterion $U_b \approx k_{\text{B}}T\,\ln(\omega_0\tau)$ is met, with ω_0 the attempt frequency for escaping the well and τ the relevant time scale of the experiment [52,53]. In order to better understand the situation in the experiment of Ref. [9], we can use these relations to find the distance $\delta r = |\boldsymbol{r} - \boldsymbol{r}_0|$ away from the boundary where the vortex leaves the pin via thermal activation. Using the estimates [9] $\omega_0 \sim 10^{11}$ Hz and $\tau \sim 300$ s, we find that $U_b \approx 30\,k_{\text{B}}T \approx 130$ K at the temperature $T = 4.2$ K of the experiment. Combining the expressions for the saddle point position (C1), for the barrier (C2) and for the displacement $u_x = F_{ac}/2\tilde{a}$, see (5), we obtain

$$\delta r \approx \left[u_x^2 + u_y^2(6U_b/F_{ac}u_x)\right]^{1/2}. \quad \text{(C3)}$$

For the escape out of the well at $x \approx 20$ nm (right edge of the central well in Fig. 2), where $(u_x, u_y) \approx (0.15, -0.05)$ nm and with $F_{ac} \approx 10^{-14}$ N, one arrives at a typical energy change per step in F_{L} of $F_{ac}u_x \approx 0.1$ K. This results in an estimate $\delta r \approx 14$ nm, an appreciable distance away from the Hessian stability boundary. Hence, one has to conclude that thermal fluctuations cut off the measured trajectory long before reaching the Hessian stability boundary, in agreement with the discussion in the experiment [9]. As a consequence, the displacements u_x and u_y, although proportional to the inverse Hessian $(4ab - c^2)^{-1}$, do not show a divergence when approaching the Hessian stability boundary, as the latter is never

closely approached. In the same vain, the vortex leaves the pin much before the force saturates at the Hessian boundary.

In principle, anharmonic effects may influence the vortex escape from the stable regions– - this is the case at small temperatures [when $U_b \gg k_B T \ln(\omega_0 \tau)$] or at large *ac* amplitudes u. Including such anharmonicities and solving for the displacement u_x, we find the periodic dynamics

$$u_x = -\frac{2b}{c} u_y = \frac{\tilde{a}}{3d}\left[\sqrt{1+\frac{3d}{\tilde{a}^2}F_{ac}e^{-i\omega t}}-1\right]e^{i\omega t}, \tag{C4}$$

as long as the *ac* amplitude F_{ac} is below the threshold

$$F_{\rm thr} \equiv \frac{\tilde{a}^2}{3|d|}. \tag{C5}$$

As the ratio $F_{ac}/F_{\rm thr}$ approaches unity, anharmonic effects manifest; in particular, the barrier decreases periodically in time to a value

$$U_b^{\rm anh} = \frac{4\tilde{a}^3}{27d^2}\left(1-\frac{F_{ac}}{F_{\rm thr}}\right)^{3/2}, \tag{C6}$$

thus allowing for a faster escape of the vortex due to the combined effect of thermal activation and anharmonicity in the *ac* response. For even larger *ac* forces, $F_{ac} > F_{\rm thr}$, the vortex is pushed over the barrier and leaves the defect for good. Expressing the ratio again through known quantities, we find that $F_{ac}/F_{\rm thr} \approx \sqrt{F_{ac}u_x/U_b}$, which, when inserting the experimental numbers [9], provides us with the value $1/20$, telling us that anharmonic effects are small for the experiment in Ref. [9].

APPENDIX D: GAUSSIAN PROBABILITY DISTRIBUTION

In the limit of strongly overlapping defects, the functional distribution function $\mathcal{P}[U(\boldsymbol{r})]$ assumes a Gaussian form, see Eqs. (25) and (26). We verify (and sharpen) this statement by studying correlators and via direct calculation of $\mathcal{P}[U(\boldsymbol{r})]$ from Eq. (23).

1. Correlators

Given a set of defect (or pin) locations $\{\boldsymbol{r}_i\}_{i=1}^N$, we define the associated density

$$\rho(\boldsymbol{r}) = \sum\nolimits_{i=1}^{N} \delta(\boldsymbol{r}-\boldsymbol{r}_i). \tag{D1}$$

When distributed homogeneously over the area Ω, the average density at the position $\boldsymbol{r}$ is

$$\langle\rho(\boldsymbol{r})\rangle = \int\left[\prod_{i=1}^{N}\frac{d^2r_i}{\Omega}\right]\rho(\boldsymbol{r}) = N/\Omega = n_p \tag{D2}$$

and the two-point correlator reads

$$\langle\rho(\boldsymbol{r})\rho(\boldsymbol{s})\rangle = N(N-1)/\Omega^2 + (N/\Omega)\,\delta(\boldsymbol{r}-\boldsymbol{s}). \tag{D3}$$

Going over to reduced densities $\bar{\rho}(r) = \rho(r) - n_p$, the first four correlators read (in the thermodynamic limit $N, \Omega \to \infty$, with $N/\Omega = n_p$)

$$\langle\bar{\rho}(\boldsymbol{r})\rangle = 0, \tag{D4a}$$

$$\langle\bar{\rho}(\boldsymbol{r})\bar{\rho}(\boldsymbol{s})\rangle = n_p\,\delta(\boldsymbol{r}-\boldsymbol{s}), \tag{D4b}$$

$$\langle\bar{\rho}(\boldsymbol{r})\bar{\rho}(\boldsymbol{s})\bar{\rho}(\boldsymbol{t})\rangle = n_p\,\delta(\boldsymbol{r}-\boldsymbol{s})\delta(\boldsymbol{r}-\boldsymbol{t}), \tag{D4c}$$

$$\begin{aligned}\langle\bar{\rho}(\boldsymbol{r})\bar{\rho}(\boldsymbol{s})\bar{\rho}(\boldsymbol{t})\bar{\rho}(\boldsymbol{x})\rangle = {}& n_p\,\delta(\boldsymbol{r}-\boldsymbol{s})\delta(\boldsymbol{r}-\boldsymbol{t})\delta(\boldsymbol{r}-\boldsymbol{x}) \\ & + n_p^2\,[\delta(\boldsymbol{r}-\boldsymbol{s})\delta(\boldsymbol{t}-\boldsymbol{x}) \\ & + \delta(\boldsymbol{r}-\boldsymbol{t})\delta(\boldsymbol{s}-\boldsymbol{x}) + \delta(\boldsymbol{r}-\boldsymbol{x})\delta(\boldsymbol{s}-\boldsymbol{t})].\end{aligned} \tag{D4d}$$

These results translate into correlators for the potential

$$U(\boldsymbol{r}) = \sum\nolimits_i V(\boldsymbol{r}-\boldsymbol{r}_i) = \int d^2x\, V(\boldsymbol{r}-\boldsymbol{x})\rho(\boldsymbol{x}) \tag{D5}$$

via simple integration: $\langle U(\boldsymbol{r})\rangle = 0$ [as $\int d^2r V(\boldsymbol{r}) = 0$] and

$$\begin{aligned}\langle U(\boldsymbol{r})U(\boldsymbol{s})\rangle &= n_p\int d^2x d^2y V(\boldsymbol{r}-\boldsymbol{x})V(\boldsymbol{s}-\boldsymbol{y})\langle\rho(\boldsymbol{x})\rho(\boldsymbol{y})\rangle \\ &= G(\boldsymbol{r}-\boldsymbol{s})\end{aligned} \tag{D6}$$

with the two-point potential correlator

$$G(\boldsymbol{r}-\boldsymbol{s}) = n_p\xi^2\int\frac{d^2x}{\xi^2}V(\boldsymbol{r}-\boldsymbol{x})V(\boldsymbol{s}-\boldsymbol{x}). \tag{D7}$$

Here, $n_p\xi^2$ takes the role of the large density parameter, with the integral remaining of order V_0^2. One easily shows that the even-order $(2k)$-point correlators are dominated by the Wick term $\propto (n_p\xi^2)^k$,

$$\begin{aligned}&\langle U(\boldsymbol{r}_1)\cdots U(\boldsymbol{r}_{2k})\rangle \\ &\quad = \sum_{\substack{\text{pairings}\\ \{p_1,\ldots,p_k\}}}\left[\prod_{\ell=1}^{k} G(\boldsymbol{r}_{p_{\ell,1}}-\boldsymbol{r}_{p_{\ell,2}})\right] + \mathcal{O}[(n_p\xi^2)^{k-1}],\end{aligned} \tag{D8}$$

with the set of pairings $\{p_1,\ldots,p_k\}$ including all sites $\boldsymbol{r}_i$ ($i \in \{1,\ldots 2k\}$). The odd-order $(2k+1)$-point correlators start with a subleading term $\propto (n_p\xi^2)^k$. Note that all subleading terms involve higher-order potential overlaps, e.g., the three-defect overlap of the form

$$G_3(\boldsymbol{r},\boldsymbol{s},\boldsymbol{t}) = n_p\xi^2\int\frac{d^2x}{\xi^2}V(\boldsymbol{r}-\boldsymbol{x})V(\boldsymbol{s}-\boldsymbol{x})V(\boldsymbol{t}-\boldsymbol{x}). \tag{D9}$$

For large densities the Wick term dominates and the distribution for $U(\boldsymbol{r})$ becomes Gaussian as $n_p\xi^2 \to \infty$.

2. Probability distribution $\mathcal{P}[U(\boldsymbol{r})]$

In order to calculate the functional probability distribution $\mathcal{P}[U(\boldsymbol{r})]$, we discretize the problem and evaluate $\mathcal{P}[\{U_\alpha\}]$ on the discrete set of lattice sites $\{\boldsymbol{r}_\alpha\}_1^M$ on a mesh with unit volume $v = a^2$, $Mv = \Omega$. Note that positions $\boldsymbol{r}$ with Latin/Greek indices denote coordinates of defects/mesh-points. The discretized probability function then derives from the measure Eq. (23),

$$\mathcal{P}[\{U_\alpha\}] = \int\left[\prod_{i=1}^{N}\frac{d^2r_i}{\Omega}\right]\left\{\prod_\beta \delta[U_\beta - U(\boldsymbol{r}_\beta)]\right\}. \tag{D10}$$

We rewrite the Dirac δ distributions in Fourier space and obtain the expression

$$\mathcal{P}[\{U_\alpha\}] = \int \left[\prod_\alpha \frac{dK_\alpha}{2\pi/v}\right]\left[\prod_i^N \frac{d^2 r_i}{\Omega}\right] e^{iv\sum_\beta K_\beta[U_\beta - U(\boldsymbol{r}_\beta)]}$$
$$= \int \left[\prod_\alpha \frac{dK_\alpha}{2\pi/v}\right] e^{iv\sum_\beta K_\beta U_\beta} \times \left[\int \frac{d^2 r}{\Omega} e^{-iv\sum_\beta K_\beta V(\boldsymbol{r}_\beta - \boldsymbol{r})}\right]^N, \quad \text{(D11)}$$

where we have made use of Eq. (D5). Adding and subtracting unity in the last square bracket, and taking the thermodynamic limit $N, \Omega \to \infty$ with $n_p = N/\Omega$, we can rewrite the above equation as

$$\mathcal{P}[\{U_\alpha\}] = \int \left[\prod_\alpha \frac{dK_\alpha}{2\pi/v}\right] e^{\psi[\{K_\alpha, U_\alpha\}; V(\boldsymbol{r})]} \quad \text{(D12)}$$

with

$$\psi[\{K_\alpha, U_\alpha\}; V(\boldsymbol{r})] = iv\sum_\beta K_\beta U_\beta + n_p v \sum_\alpha [e^{-iv\sum_\beta K_\beta V(\boldsymbol{r}_\beta - \boldsymbol{r}_\alpha)} - 1]. \quad \text{(D13)}$$

For consistency, we have discretized the average over defect positions $\int d^2 r \to v\sum_\alpha$. The saddle-point equation $\partial\psi/\partial K_\beta = 0$ for a given K_β reads

$$U_\beta = n_p v \sum_\alpha V(\boldsymbol{r}_\beta - \boldsymbol{r}_\alpha) e^{-iv\sum_\gamma K_\gamma V(\boldsymbol{r}_\gamma - \boldsymbol{r}_\alpha)}. \quad \text{(D14)}$$

We expand the exponential function above assuming its argument to be small, an assumption that will be validated *a posteriori* below, and find

$$U_\beta \approx n_p v \sum_\alpha V(\boldsymbol{r}_\beta - \boldsymbol{r}_\alpha) - i n_p v^2 \sum_{\alpha,\gamma} K_\gamma V(\boldsymbol{r}_\beta - \boldsymbol{r}_\alpha) V(\boldsymbol{r}_\gamma - \boldsymbol{r}_\alpha) - n_p v^3 \sum_{\alpha,\gamma,\delta} K_\gamma K_\delta V(\boldsymbol{r}_\beta - \boldsymbol{r}_\alpha) V(\boldsymbol{r}_\gamma - \boldsymbol{r}_\alpha) V(\boldsymbol{r}_\delta - \boldsymbol{r}_\alpha). \quad \text{(D15)}$$

The first term on the right-hand side is the potential's mean value, which we have assumed to vanish. For the second term in the expression above, we introduce

$$G_{\beta,\gamma} = n_p v \sum_\alpha V(\boldsymbol{r}_\beta - \boldsymbol{r}_\alpha) V(\boldsymbol{r}_\gamma - \boldsymbol{r}_\alpha), \quad \text{(D16)}$$

the discrete version of the two-point correlator (D7). With $G_{\beta,\gamma}$ of the scale $(n_p\xi^2)V_0^2$ and decaying on a length $|\boldsymbol{r}_\beta - \boldsymbol{r}_\gamma| \sim \xi$, we arrive at the estimate

$$\bar{K}_\beta \equiv v \sum_{\gamma, |\boldsymbol{r}_\beta - \boldsymbol{r}_\gamma| < \xi} K_\gamma \sim \frac{U_\beta}{(n_p\xi^2)V_0^2}. \quad \text{(D17)}$$

Substituting this estimate in the third term of Eq. (D15), we find that it is small when

$$V_0 \bar{K}_\beta \ll 1. \quad \text{(D18)}$$

The width of the distribution function for the expectation value of the potential grows only with $(n_p\xi^2)^{1/2}V_0$, what tells us that in the limit $n_p\xi^2 \to \infty$, the above condition is satisfies almost everywhere [except for far-distant tails: For $U \sim V_0 n_p \xi^2$, see (D17) and (D18), the probability has dropped to $\exp(-U^2/G) \sim \exp(-\text{const.}\, n_p\xi^2)$]. This reasoning justifies the truncation of (D15) to include only terms up to linear order in K. At the same time, it validates the assumption used after Eq. (D14) and allows to expand the exponential in (D13) to quadratic order in K. We thus arrive at the simple expression

$$\mathcal{P}[\{U_\alpha\}] \approx \int \left[\prod_\alpha \frac{dK_\alpha}{2\pi/v}\right] e^{iv\sum_\beta K_\beta U_\beta} e^{-\frac{1}{2}v^2 \sum_{\beta,\gamma} K_\beta G_{\beta,\gamma} K_\gamma} \quad \text{(D19)}$$

for the discretized probability distribution, a result that becomes exact for $n_p\xi^2 \to \infty$. Computing the Gaussian integrals over K, we find that

$$\mathcal{P}[\{U_\alpha\}] \propto e^{-\frac{1}{2}\sum_{\beta,\gamma} U_\beta (G^{-1})_{\beta,\gamma} U_\gamma}, \quad \text{(D20)}$$

where we have used the discrete version of the inversion identity $\int d^2x\, G(\boldsymbol{r} - \boldsymbol{x})\, G^{-1}(\boldsymbol{r}' - \boldsymbol{x}) = \delta(\boldsymbol{r} - \boldsymbol{r}')$, i.e.,

$$v\sum_\beta G_{\alpha,\beta}(G^{-1})_{\beta,\gamma} = \delta_{\alpha,\gamma}/v. \quad \text{(D21)}$$

Returning back to the continuum notation, we arrive at the final result

$$\mathcal{P}[U(\boldsymbol{r})] \to \mathcal{P}_G[U(\boldsymbol{r})] \equiv \frac{1}{\mathcal{Z}} e^{-\frac{1}{2}\int \frac{d^2r}{\Omega}\frac{d^2r'}{\Omega} U(\boldsymbol{r}) G^{-1}(\boldsymbol{r} - \boldsymbol{r}') U(\boldsymbol{r}')}, \quad \text{(D22)}$$

where $\mathcal{Z}$ accounts for the correct normalization. Note that more terms in the expansion of (D13) need to be retained if one is interested in properties away from the body of the probability distribution, at least in principle.

APPENDIX E: PARABOLIC TRAPS

The determination of the probability distribution $p(\mathfrak{D}, \mathfrak{T})$ of the Hessian determinant and trace for a landscape made from cut parabolas makes use of Eqs. (29) and (23), from which follows that

$$\pi(a,b,c) = \int \left[\prod_{j=1}^N \frac{d^2 r_j}{\Omega}\right] \delta[U_{xx}(0) - 2a] \times \delta[U_{yy}(0) - 2b]\, \delta[U_{xy}(0) - c]. \quad \text{(E1)}$$

Rewriting the delta distributions in Fourier space, and expressing the potential $U(\boldsymbol{r})$ through the sum of individual defect potentials $V(\boldsymbol{r} - \boldsymbol{r}_i)$, we obtain the expression

$$\pi(a,b,c) = \int \frac{dk\, dl\, dm}{(2\pi)^3} e^{i(2ka + 2lb + mc)} \times \left[\int \frac{d^2 r}{\Omega} e^{-i[kV_{xx}(\boldsymbol{r}) + lV_{yy}(\boldsymbol{r}) + mV_{xy}(\boldsymbol{r})]}\right]^N. \quad \text{(E2)}$$

In the thermodynamic limit, $N, \Omega \to \infty$ at fixed defect density $n_p = N/\Omega$, the last factor can be rewritten as

$$\left[1 + \frac{n_p}{N}\epsilon(k,l,m)\right]^N = e^{n_p \epsilon(k,l,m)} \quad \text{(E3)}$$

with $\epsilon(k,l,m)$ involving only the potential shape $V(\boldsymbol{r})$ of an individual defect,

$$\epsilon(k,l,m) = \int d^2r\left[e^{-i[kV_{xx}(\boldsymbol{r})+lV_{yy}(\boldsymbol{r})+mV_{xy}(\boldsymbol{r})]}-1\right]. \tag{E4}$$

As a result, we arrive at the compact form

$$\pi(a,b,c) = \int \frac{dk\,dl\,dm}{(2\pi)^3} e^{i(2ka+2lb+mc)} e^{n_p\epsilon(k,l,m)}. \tag{E5}$$

While the above procedure applies for all defect types, we explicitly evaluate the above expressions for the cut parabolic defect. Since all second derivatives of $V(\boldsymbol{r})$ are either $2V_0/\xi^2$ or zero, Eq. (E4) reads

$$\epsilon(k,l,m) = \Omega_0\left[e^{-i2V_0(k+l)/\xi^2}-1\right]. \tag{E6}$$

Inserting this result into Eq. (E5), expanding the last factor in a power series, and using the binomial theorem, we find that

$$\pi(a,b,c) = \int \frac{dk\,dl\,dm}{(2\pi)^3} e^{i(2ka+2lb+mc)} \times \sum_{\nu=0}^{\infty}\sum_{\mu=\nu}^{\infty} \frac{(n_p\Omega_0)^\mu}{\nu!(\mu-\nu)!} e^{-i2V_0\nu(k+l)/\xi^2}(-1)^{\mu-\nu}. \tag{E7}$$

The integrations over k,l,m provide δ distributions and rearranging terms in the sum, we obtain

$$\pi(a,b,c) = \sum_{\nu=0}^{\infty} \delta[\nu(2V_0/\xi^2)-2a]\,\delta[\nu(2V_0/\xi^2)-2b] \times \delta(c)\,\mathrm{Poiss}(\nu, n_p\Omega_0). \tag{E8}$$

As expected, the Hessian matrix can only take on discrete values $(2\nu V_0/\xi^2)\,\mathbb{I}$ and, correspondingly, the probability distribution is a sum of δ distributions.

Next, we make use of the result for $\pi(a,b,c)$, Eq. (E8), in the determination of the probability distribution $p(\mathfrak{D},\mathfrak{T})$ for a Hessian H with $\det H = \mathfrak{D}$ and $\mathrm{tr}H = \mathfrak{T}$, see Eq. (22). The expression (28) for $p(\mathfrak{D})$ generalizes to

$$p(\mathfrak{D},\mathfrak{T}) = \int_{-\infty}^{\infty} da \int_{-\infty}^{\infty} db \int_{-\infty}^{\infty} dc\,\pi(a,b,c) f(a,b,c;\mathfrak{D},\mathfrak{T}) \tag{E9}$$

with

$$f(a,b,c;\mathfrak{D},\mathfrak{T}) = \delta[4ab-c^2-\mathfrak{D}]\,\delta[2a+2b-\mathfrak{T}]. \tag{E10}$$

and inserting the result Eq. (E8) for $\pi(a,b,c)$, we find

$$p(\mathfrak{D},\mathfrak{T}) = \sum_{\nu=0}^{\infty} \mathrm{Poiss}(\nu, n_p\Omega_0)\delta[\nu^2(2V_0/\xi^2)^2-\mathfrak{D}] \times \delta[\nu(2V_0/\xi^2)-\mathfrak{T}]. \tag{E11}$$

The final integration over strictly positive $\mathfrak{D}$ and $\mathfrak{T}$ results in the stable area fraction of the Hessian map, $\mathcal{C}_{\mathrm{pos}} = 1 - \mathrm{Poiss}(0, n_p\Omega_0)$.

[1] A. Tonomura, H. Kasai, O. Kamimura, T. Matsuda, K. Harada, Y. Nakayama, J. Shimoyama, K. Kishio, T. Hanaguri, K. Kitazawa *et al.*, Observation of individual vortices trapped along columnar defects in high-temperature superconductors, Nature (London) **412**, 620 (2001).

[2] S. J. Bending, Local magnetic probes of superconductors, Adv. Phys. **48**, 449 (1999).

[3] J. R. Kirtley, Fundamental studies of superconductors using scanning magnetic imaging, Rep. Prog. Phys. **73**, 126501 (2010).

[4] H. Suderow, I. Guillamón, J. G. Rodrigo, and S. Vieira, Imaging superconducting vortex cores and lattices with a scanning tunneling microscope, Supercond. Sci. Technol. **27**, 063001 (2014).

[5] L. Thiel, D. Rohner, M. Ganzhorn, P. Appel, E. Neu, B. Müller, R. Kleiner, D. Koelle, and P. Maletinsky, Quantitative nanoscale vortex imaging using a cryogenic quantum magnetometer, Nat. Nanotechnol. **11**, 677 (2016).

[6] E. W. J. Straver, J. E. Hoffman, O. M. Auslaender, D. Rugar, and K. A. Moler, Controlled manipulation of individual vortices in a superconductor, Appl. Phys. Lett. **93**, 172514 (2008).

[7] O. M. Auslaender, L. Luan, E. W. J. Straver, J. E. Hoffman, N. C. Koshnick, E. Zeldov, D. A. Bonn, R. Liang, W. N. Hardy, and K. A. Moler, Mechanics of individual isolated vortices in a cuprate superconductor, Nat. Phys. **5**, 35 (2009).

[8] A. Kremen, S. Wissberg, N. Haham, E. Persky, Y. Frenkel, and B. Kalisky, Mechanical control of individual superconducting vortices, Nano Lett. **16**, 1626 (2016).

[9] L. Embon, Y. Anahory, A. Suhov, D. Halbertal, J. Cuppens, A. Yakovenko, A. Uri, Y. Myasoedov, M. L. Rappaport, M. E. Huber *et al.*, Probing dynamics and pinning of single vortices in superconductors at nanometer scales, Sci. Rep. **5**, 7598 (2015).

[10] L. Embon, Y. Anahory, Ž. L. Jelić, E. O. Lachman, Y. Myasoedov, M. E. Huber, G. P. Mikitik, A. V. Silhanek, M. V. Milošević, A. Gurevich, and E. Zeldov, Imaging of super-fast dynamics and flow instabilities of superconducting vortices, Nat. Commun. **8**, 85 (2017).

[11] W.-K. Kwok, U. Welp, A. Glatz, A. E. Koshelev, K. J. Kihlstrom, and G. W. Crabtree, Vortices in high-performance high-temperature superconductors, Rep. Prog. Phys. **79**, 116501 (2016).

[12] I. A. Sadovskyy, Y. Jia, M. Leroux, J. Kwon, H. Hu, L. Fang, C. Chaparro, S. Zhu, U. Welp, J.-M. Zuo *et al.*, Toward superconducting critical current by design, Adv. Mater. **28**, 4593 (2016).

[13] M. Baert, V. V. Metlushko, R. Jonckheere, V. V. Moshchalkov, and Y. Bruynseraede, Flux-Line Lattices Stabilized in Superconducting Films by a Regular Array of Artificial Defects, Phys. Rev. Lett. **74**, 3269 (1995).

[14] J. I. Martín, M. Vélez, J. Nogués, and I. K. Schuller, Flux Pinning in a Superconductor by an Array of Submicrometer Magnetic Dots, Phys. Rev. Lett. **79**, 1929 (1997).

[15] M. J. Van Bael, J. Bekaert, K. Temst, L. Van Look, V. V. Moshchalkov, Y. Bruynseraede, G. D. Howells, A. N. Grigorenko, S. J. Bending, and G. Borghs, Local Observation of Field Polarity Dependent Flux Pinning by Magnetic Dipoles, Phys. Rev. Lett. **86**, 155 (2001).

[16] L. Chibotaru, A. Ceulemans, V. Bruyndoncx, and V. Moshchalkov, Symmetry-induced formation of antivortices in mesoscopic superconductors, Nature (London) **408**, 833 (2000).

[17] I. V. Grigorieva, W. Escoffier, J. Richardson, L. Y. Vinnikov, S. Dubonos, and V. Oboznov, Direct Observation of Vortex Shells and Magic Numbers in Mesoscopic Superconducting Disks, Phys. Rev. Lett. **96**, 077005 (2006).

[18] H. Zhao, V. Misko, F. Peeters, S. Dubonos, V. Oboznov, and I. Grigorieva, Vortex configurations in mesoscopic superconducting triangles: Finite-size and shape effects, Europhys. Lett. **83**, 17008 (2008).

[19] J. Sánchez, G. Rumi, R. Maldonado, N. Bolecek, J. Puig, P. Pedrazzini, G. Nieva, M. Dolz, M. Konczykowski, C. van der Beek *et al.*, Non-Gaussian tail in the force distribution: A hallmark of correlated disorder in the host media of elastic objects, Sci. Rep., **10**, 19452 (2020).

[20] https://en.wikipedia.org/wiki/Ball-in-a-maze_puzzle (last checked 17 Feb., 2022).

[21] C. Reichhardt, C. J. Olson, J. Groth, S. Field, and F. Nori, Microscopic derivation of magnetic-flux-density profiles, magnetization hysteresis loops, and critical currents in strongly pinned superconductors, Phys. Rev. B **52**, 10441 (1995).

[22] C. J. Olson Reichhardt, Y. L. Wang, Z. L. Xiao, W.-K. Kwok, D. Ray, C. Reichhardt, and B. Jankó, Pinning, flux diodes and ratchets for vortices interacting with conformal pinning arrays, Physica C **533**, 148 (2017).

[23] T. Halpin-Healy and Y.-C. Zhang, Kinetic roughening phenomena, stochastic growth, directed polymers and all that. Aspects of multidisciplinary statistical mechanics, Phys. Rep. **254**, 215 (1995).

[24] G. Blatter, M. V. Feigel'man, V. B. Geshkenbein, A. I. Larkin, and V. M. Vinokur, Vortices in high-temperature superconductors, Rev. Mod. Phys. **66**, 1125 (1994).

[25] T. Giamarchi and P. Le Doussal, Elastic theory of flux lattices in the presence of weak disorder, Phys. Rev. B **52**, 1242 (1995).

[26] T. Nattermann and S. Scheidl, Vortex-glass phases in type-II superconductors, Adv. Phys. **49**, 607 (2000).

[27] A. J. Bray and D. S. Dean, Statistics of Critical Points of Gaussian Fields on Large-Dimensional Spaces, Phys. Rev. Lett. **98**, 150201 (2007).

[28] Y. V. Fyodorov and P. L. Doussal, Hessian spectrum at the global minimum of high-dimensional random landscapes, J. Phys. A: Math. Theor. **51**, 474002 (2018).

[29] I. Freund, Saddles, singularities, and extrema in random phase fields, Phys. Rev. E **52**, 2348 (1995).

[30] A. Weinrib and B. I. Halperin, Distribution of maxima, minima, and saddle points of the intensity of laser speckle patterns, Phys. Rev. B **26**, 1362 (1982).

[31] A. Annibale, A. Cavagna, I. Giardina, and G. Parisi, Supersymmetric complexity in the Sherrington-Kirkpatrick model, Phys. Rev. E **68**, 061103 (2003).

[32] J. Pearl, Current distribution in superconducting films carrying quantized fluxoids, Appl. Phys. Lett. **5**, 65 (1964).

[33] D. Ertaş and D. R. Nelson, Irreversibility, mechanical entanglement and thermal melting in superconducting vortex crystals with point impurities, Physica C **272**, 79 (1996).

[34] G. Blatter and V. Geshkenbein, *Superconductivity*, edited by K. Bennemann and J. Ketterson (Springer-Verlag, Berlin, 2008).

[35] E. Frey, D. R. Nelson, and D. S. Fisher, Interstitials, vacancies, and supersolid order in vortex crystals, Phys. Rev. B **49**, 9723 (1994).

[36] V. Vinokur, B. Khaykovich, E. Zeldov, M. Konczykowski, R. Doyle, and P. Kes, Lindemann criterion and vortex-matter phase transitions in high-temperature superconductors, Physica C **295**, 209 (1998).

[37] J. Kierfeld and V. Vinokur, Lindemann criterion and vortex lattice phase transitions in type-II superconductors, Phys. Rev. B **69**, 024501 (2004).

[38] A. Schönenberger, A. Larkin, E. Heeb, V. Geshkenbein, and G. Blatter, Strong Pinning and Plastic Deformations of the Vortex Lattice, Phys. Rev. Lett. **77**, 4636 (1996).

[39] M. Yamada and A. Vilenkin, Hessian eigenvalue distribution in a random Gaussian landscape, J. High Energy Phys. 03 (2018) 029.

[40] J. Zinn-Justin, *Path Integrals in Quantum Mechanics* (Oxford University Press, Oxford, 2005).

[41] A. Altland and B. D. Simons, *Condensed Matter Field Theory*, 2nd ed. (Cambridge University Press, Cambridge, 2010).

[42] J. Craig, A new, simple and exact result for calculating the probability of error for two-dimensional signal constellations, in *MILCOM 91 - Conference record*, Vol. 2 (1991) p. 571.

[43] R. Labusch, Calculation of the critical field gradient in type-II superconductors, Cryst. Lattice Defects **1**, 1 (1969).

[44] A. I. Larkin and Y. N. Ovchinnikov, Pinning in type-II superconductors, J. Low Temp. Phys. **34**, 409 (1979).

[45] G. Blatter, V. B. Geshkenbein, and J. A. G. Koopmann, Weak to Strong Pinning Crossover, Phys. Rev. Lett. **92**, 067009 (2004).

[46] M. Buchacek, V. B. Geshkenbein, and G. Blatter, Role of rare events in the pinning problem, Phys. Rev. Research **2**, 043266 (2020).

[47] A. Tanguya and T. Vettorel, From weak to strong pinning: A finite size study, Eur. Phys. J. B **38**, 71 (2004).

[48] X. Cao, S. Bouzat, A. B. Kolton, and A. Rosso, Localization of soft modes at the depinning transition, Phys. Rev. E **97**, 022118 (2018).

[49] F. Gaggioli, G. Blatter, M. Buchacek, and V. Geshkenbein, Strong pinning transition with arbitrary defect potentials (unpublished).

[50] J. Bardeen and M. J. Stephen, Theory of the motion of vortices in superconductors, Phys. Rev. **140**, A1197 (1965).

[51] H. Montgomery, The thermal conductivity of lead at low temperatures, Proc. R. Soc. London A 244, 85 (1958).

[52] H. A. Kramers, Brownian motion in a field of force and the diffusion model of chemical reactions, Physica **7**, 284 (1940).

[53] P. Hänggi, P. Talkner, and M. Borkovec, Reaction-rate theory: Fifty years after Kramers, Rev. Mod. Phys. **62**, 251 (1990).